

## **ABSTRACT**

PROPST, ADAM CHRISTOPHER. Damage Monitoring in Woven Composites Using Fiber-Bragg Grating Sensors on Multiple Time Scales. (Under the direction of Dr. K. J. Peters).

This study investigates the application of Fiber Bragg Grating (FBG) optical sensors interrogation techniques over several time scales to monitor damage in composite structures due to low velocity impacts events. Optical fiber sensors are embedded into carbon fiber/epoxy resin woven composites using a single-step cure process. The composite specimens are subjected to multiple low energy impacts until failure. Impact events are characterized by acceleration and position sensors integral to the impactor head. The embedded FBG sensors are interrogated using three different interrogation techniques. Low speed, full spectrum measurements are recorded using a tunable laser source. High speed, peak wavelength detection data is taken using a commercial peak wavelength interrogation system. Finally, high speed full spectrum measurements are recorded using new instrumentation developed at Brigham Young University. By qualitatively examining the responses of these three techniques and comparing the FBG data with impact characterization data, a more complete picture of the composite health is available.

Damage Monitoring in Woven Composites Using Fiber-Bragg  
Grating Sensors on Multiple Time Scales

by  
Adam Christopher Propst

A thesis submitted to the Graduate Faculty of  
North Carolina State University  
In partial fulfillment of the  
Requirements for the Degree of  
Master of Science

Aerospace Engineering

Raleigh, North Carolina

2009

APPROVED BY:

---

Dr. M. A Zikry

---

Dr. M. K. Ramasubramanian

---

Dr. K. J. Peters  
Chair of Advisory Committee

## **BIOGRAPHY**

Adam Propst was born in Statesville, NC on January 14, 1983 to Brad and Julie Propst. As he grew up, Adam was always captivated by science and technology, spending many hours reading books on a variety of topics and exploring the world around him. While at Troutman Middle School in Troutman, NC, he fell in love with music and began playing the trombone. He attended Freedom High School in Morganton, NC, where he was president of the Science Olympiad Team and played in the Marching Band, Wind Ensemble, and Jazz Band. In 2000, Adam was selected to attend the Governor's School of North Carolina, focusing on orchestral music.

Beginning in 1997, Adam began his hobby of building and flying remote control airplanes. The wonders of flight led him to study aerospace engineering at North Carolina State University, where he received the Clarence M. Smith, Jr., Edward E. Hood, Jr., and James M. Johnston Scholarships. During his time as an undergraduate, Adam was active in the Aerial Robotics Club, serving as Vice President and flight test pilot. He completed his bachelor's degree in Aerospace Engineering in December 2006. Adam was inducted into Sigma Gamma Tau aerospace honor society in 2007. He continued his education at NCSU by working towards his master's degree in aerospace engineering under the direction of Dr. Kara Peters. His research focused on expanding damage monitoring techniques by using full-spectrum measurements of optical sensors embedded in woven composites. Adam completed his master's degree in aerospace engineering in May 2009.

## ACKNOWLEDGMENTS

Adam would like to recognize the support, encouragement, and guidance provided by his advisor, Dr. Kara Peters, who kept him focused and motivated. Adam would also like to thank Dr. Mohammed Zikry and Dr. M. K. Ramasubramanian, members of his advisory committee. Adam would like to thank Dr. Richard Selfridge, Dr. Steve Schultz, and Wesley Kunzler of the Department of Electrical and Computer Engineering at Brigham Young University, who made this research possible by generously providing their time, expertise, and interrogation equipment to help gather the high speed full spectrum data presented in this study.

Adam would like to acknowledge the financial support from the Air Force Office of Scientific Research through grant # FA9550-0801-0017 and program manager Victor Giurgiutiu. Also, he would like to acknowledge the Photonics Technology Access Program, funded by the National Science Foundation and the Defense Advanced Research Projects Agency, for providing the Micron Optics SM-130 high speed peak detection interrogator.

Adam would like to recognize Adam Parker and Zachary Capps for their many hours of assistance in this study fabricating and testing composite specimens and processing data, as well as Chun Park for his input. Additionally, Adam would like to thank his family and friends, whose prayers and encouragement have supported him through all of his endeavors in life.

## TABLE OF CONTENTS

LIST OF TABLES.....	vi
LIST OF FIGURES .....	vii
Chapter 1. Introduction .....	1
1.1 Overview .....	1
1.2 Motivation.....	2
1.3 Background .....	4
Chapter 2. Experimental Methods .....	8
2.1 Sample Preparation .....	8
2.2 Impact Testing .....	11
2.3 FBG Sensor Interrogation.....	13
2.3.1 Low speed, full-spectrum.....	13
2.3.2 High speed, peak wavelength detection.....	14
2.3.3 High speed, full-spectrum.....	14
Chapter 3. Experimental Results and Analysis .....	22
3.1 Low speed, full spectrum data .....	22
3.2 High speed, peak wavelength data.....	25
3.3 High speed, full spectrum data.....	27
3.3.2 Sample BY-1 .....	29
3.3.1 Sample BY-2 .....	32
3.3.3 Sample BY-3 .....	35
3.3.4 Sample BY-4 .....	37

Chapter 4. Conclusions .....	67
REFERENCES.....	70
APPENDICES.....	72
APPENDIX A – MATLAB Code for Reducing NCSU Drop Tower Position and Acceleration Sensor Impact Characterization Data .....	73
APPENDIX B – MATLAB Code for Reducing High Speed, Full Spectrum Data (BY-1)	74
APPENDIX C – MATLAB Code for Reducing High Speed, Full Spectrum Data (BY-2 – BY-4) .....	76
APPENDIX D – MATLAB Code for Processing and Displaying High Speed, Full Spectrum Data.....	82

## LIST OF TABLES

Table 2.1. Samples produced for this testing with embedded fiber Bragg gratings and their specifications.....	19
Table 3.1. Samples with FBG sensors interrogated using BYU's FSIM instrumentation. ...	46

## LIST OF FIGURES

Figure 1.1. Map of spatial and temporal scales for graphite-epoxy woven composite laminate damage resulting from impacts. Time and length scale values are estimated from previous experimental data obtained at NCSU.....	7
Figure 1.2. Baseline FBG response and responses due to various loading cases: (a) no load case, (b) uniform axial load, (c) transverse compressive load, (d) non-uniform applied strain field, (e) damaged sensor ( <i>Pearson, et al. 2007</i> ).....	7
Figure 2.1. Embedded fiber specimen prior to curing cycle with Mylar release film, peel ply, and putty in place and ready to receive upper peel-ply layers, and vacuum tubing before sealing and applying vacuum.....	17
Figure 2.2. Cross section of specimen layup at embedded optical fiber showing overlapping peel-ply, protective putty, fiber, lamina, and outer mylar layers (not to scale).....	17
Figure 2.3. Layout and dimensions of specimen with embedded Fiber Bragg Grating. ....	18
Figure 2.4. Composite specimen with fabrication materials and excess epoxy removed and ready to be installed in the impact tower. ....	18
Figure 2.5. Specimen with embedded FBG sensor mounted in instrumented drop tower. ....	20
Figure 2.6. Micron Optics SM130 high speed peak-detecting optical interrogator.....	20
Figure 2.7. FSIM high speed full spectrum optical interrogator developed at BYU.....	21
Figure 3.1 Low speed, full spectrum data for embedded sensor before and after impact damage (S-3, strike 00 and strike 08). ....	39
Figure 3.2 Low speed, full spectrum data for sample S-4 (sensor failed on strike 30 of 79). For this and all later spectral sweep plots, red indicates maximum intensity; dark blue indicates minimum intensity. ....	39
Figure 3.3 Contact force between impactor and the sample (top) and energy dissipated over the life of the sample (bottom) for S-4.....	40
Figure 3.4 Low speed, full spectrum data for sample S-6. ....	41
Figure 3.5 Contact force between impactor and the sample (top) and energy dissipated over the life of the sample (bottom) for S-6.....	42

Figure 3.6 Low speed, full spectrum data for sample S-7. ....	43
Figure 3.7 Contact force between impactor and the sample (top) and energy dissipated over the life of the sample (bottom) for S-7.....	44
Figure 3.8 High speed, peak wavelength data showing typical FBG response (S-1, strike #36). ....	45
Figure 3.9 High speed, peak wavelength data showing the Bragg wavelength 50ms before (blue) and 50ms after (red) the impact event, along with the Bragg wavelength at the point of maximum shift during the event itself (black) for sample S-1. ....	45
Figure 3.10 Contact force between impactor and the sample (top) and energy dissipated over the life of the sample (bottom) for S-1. Dissipated energy data was not collected for strikes 1-3. ....	46
Figure 3.11 High speed, full spectrum raw data (top) showing a single frequency sweep in the continuous data stream capturing the reference and embedded FBGs and the flyback responses between this sweep and the sweeps preceding and following it. The corresponding saw-tooth scanning pattern of the MEMS filter (bottom) falls between approximately 1530nm and 1560nm. The main sweeps are colored green while the flybacks are colored red (BY-1, strike #05). ....	47
Figure 3.12 High speed, full spectrum raw and filtered data showing the reference and embedded grating responses in a single frequency sweep (BY-1, strike #05). ....	47
Figure 3.13 Full image of high speed, full spectrum data for a single strike showing the reference grating on the left and the embedded grating response on the right (BY-1, strike #19). ....	48
Figure 3.14 Close-up image of high speed, full spectrum data for at the time of impact for a single strike showing only the embedded grating response (BY-1, strike #19). ....	48
Figure 3.15 High speed, full spectrum raw and filtered data showing the reference and embedded grating responses in a single frequency sweep (BY-2, strike #01). ....	49
Figure 3.16 Full image of high speed, full spectrum data for a single strike showing reference grating on the left and the embedded grating response on the right (BY-2, strike #01). ....	49
Figure 3.17 Close-up image of high speed, full spectrum data for at the time of impact for a single strike showing only the embedded grating response (BY-2, strike #01). ....	50
Figure 3.18 Image of strike #07 response for sample BY-1. ....	51

Figure 3.19 Image of strike #09 response for sample BY-1.....	51
Figure 3.20 Image of strike #12 response for sample BY-1.....	51
Figure 3.21 Image of strike #15 response for sample BY-1.....	51
Figure 3.22 Images of responses for strikes 11 through 15 (from top to bottom) for sample BY-1 showing secondary response at wavelengths several nanometers longer than the primary response. Each image shows 150ms before and 200ms after the initial FBG response during the strike event. The horizontal axes show wavelength shift (nm) from an initial reference point prior to damage.....	52
Figure 3.23 Image of strike #19 response for sample BY-1.....	53
Figure 3.24 Images of responses during strikes 20, 22, 28, and 29 for sample BY-1 (from top to bottom) showing relaxation. Each image shows 40ms before and 110ms after the initial FBG response during the strike event. The horizontal axes show wavelength shift (nm) from an initial reference point prior to damage.....	53
Figure 3.25 Contact force between impactor and the sample (top) and energy dissipated over the life of the sample (bottom) for BY-1. ....	54
Figure 3.26. Image of strike #03 response for sample BY-2.....	55
Figure 3.27. Image of strike #20 response for sample BY-2.....	55
Figure 3.28. Image of strike #29 response for sample BY-2.....	55
Figure 3.29. Image of strike #65 response for sample BY-2.....	55
Figure 3.30. Progression of FBG relaxation responses during strikes 67, 77, 79, and 81 (from top to bottom) for sample BY-2. Each image shows 20ms before and 50ms after the initial FBG response during the strike event. The horizontal axes show wavelength shift (nm) from an initial reference point before each strike.....	56
Figure 3.31. Oscillatory FBG responses during strikes 6, 15, 39, 42, and 53 (from top to bottom) for sample BY-2. Each image shows 15ms before and 35ms after the initial FBG response during the strike event. The horizontal axes show wavelength shift (nm) from an initial reference point before each strike.....	57
Figure 3.32. Oscillatory FBG responses during strikes 61, 64, 68, and 77 (from top to bottom) for sample BY-2. Each image shows 15ms before and 35ms after the initial FBG response during the strike event. The horizontal axes show wavelength shift (nm) from an initial reference point before each strike.....	58

Figure 3.33 Contact force between impactor and the sample (top) and energy dissipated over the life of the sample (bottom) for BY-2. ....	59
Figure 3.34 Image of strike #02 response for sample BY-3. ....	59
Figure 3.35 Image of strike #04 response for sample BY-3. ....	60
Figure 3.36 Image of strike #05 response for sample BY-3. ....	60
Figure 3.37 Image of strike #11 response for sample BY-3. ....	60
Figure 3.38 Image of strike #12 response for sample BY-3. ....	60
Figure 3.39 Wide bandwidth image of post-strike #09 response for sample BY-3. ....	61
Figure 3.40 Contact force between impactor and the sample (top) and energy dissipated over the life of the sample (bottom) for BY-3. ....	61
Figure 3.41 Image of strike #01 response for sample BY-4. ....	62
Figure 3.42 Image of strike #06 response for sample BY-4. ....	62
Figure 3.43 Image of strike #24 response for sample BY-4. ....	62
Figure 3.44 Image of strike #26 response for sample BY-4. ....	63
Figure 3.45 Image of strike #48 response for sample BY-4. ....	63
Figure 3.46 Image of strike #49 response for sample BY-4. ....	63
Figure 3.47 Image of responses for strikes 05 through 13 (from top to bottom) for sample BY-4 showing secondary response at wavelengths several nanometers longer than the primary response. Each image shows 125ms before and 125ms after the initial FBG response during the strike event. The horizontal axes show wavelength shift (nm) from an initial reference point prior to damage. ....	64
Figure 3.48 Image of responses for strikes 14 through 22 (from top to bottom) for sample BY-4 showing secondary response at wavelengths several nanometers longer than the primary response. Each image shows 125ms before and 125ms after the initial FBG response during the strike event. The horizontal axes show wavelength shift (nm) from an initial reference point prior to damage. ....	65
Figure 3.49 Contact force between impactor and the sample (top) and energy dissipated over the life of the sample (bottom) for BY-4. ....	66

# Chapter 1. Introduction

## 1.1 Overview

This study investigates the application of Fiber Bragg Grating (FBG) optical sensors interrogation techniques over several time scales to monitor damage in composite structures due to low velocity impacts events. Optical fiber sensors are embedded into carbon fiber/epoxy resin woven composites using a single-step cure process. The composite specimens are subjected to multiple low energy impacts until failure. Impact events are characterized by acceleration and position sensors integral to the impactor head. The embedded FBG sensors are interrogated using three different interrogation techniques. Low speed, full spectrum measurements are recorded using a tunable laser source. High speed, peak wavelength detection data is taken using a commercial peak wavelength interrogation system. Finally, high speed full spectrum measurements are recorded using new instrumentation developed at Brigham Young University. By qualitatively examining the responses of these three techniques and comparing the FBG data with impact characterization data, a more complete picture of the composite health is available.

Chapter 1 introduces lists the motivation for this study and provides an overview of the structural health monitoring (SHM) using fiber Bragg gratings as well as a census of the state of the art in the field. Chapter 2 describes the experiment equipment and methods used in this study, while Chapter 3 presents the data gathered by each FBG interrogation technique along with comparison and analysis of the results. Chapter 4 discusses the conclusions from

this study and proposes future work to further improve SHM techniques using the interrogation methods contained in this study.

## **1.2 Motivation**

Structural designers are being pushed to design components that are lighter, stronger, and tailor-made for aerospace, military, and commercial applications. Consequently, composite structures are becoming more prevalent. While composites are capable of improving performance over traditional utilized materials, they bring new challenges in their applications. The behavior of traditional metal structures is well understood and the metal materials used are highly uniform, allowing for regular inspection schedules to identify signs of impending failure and allow for preventative maintenance and the retirement of weakened components well before they fail. Composites, however, are not as well controlled in their manufacturing processes and it is far more difficult to predict their failure. During impact events, metallic structures will undergo localized plastic deformation and cracking on the surface of the structure, making damage readily apparent. On the other hand, composites often sustain damage in the interior of the laminate that is not visible during visual inspection. Low velocity impacts are prone to cause this type of hidden damage, typically referred to as barely visible impact damage. Examples of high-risk scenarios are bird-strikes on composite wind turbine blades, automotive body panels and structures in normal use, and aircraft components. While aircraft components are subject to high velocity impacts during flight, they are exposed to low velocity strikes, most notably from tools and equipment during ground handling and service.

By employing structural health monitoring techniques in composite structures, the necessary inspection frequency can be significantly reduced, saving valuable time and money for the owner of the structure. Additionally, internal damage that may go completely unnoticed during visual inspections can be detected before the integrity of the component is compromised. Thus, the safety and cost of utilizing composite materials in structures is improved.

Damage in composites due to low velocity impacts occurs over a large range of time and length scales. In Figure 1.1, the spatial-temporal regions in which the various modes of damage occur are represented for woven graphite-epoxy laminates. Damage types include short duration events such as fiber breakage and matrix cracking, longer duration matrix relaxation and delamination. The quasi-static post-impact residual stress states are obtained once the material system has reached equilibrium in the seconds and minutes following damage events. These damage types and their order of progression all play a role in the overall health of the composite. As such, monitoring of the structure should include measurements over the full range of damage-related lengths and durations in order to fully characterize the composite health.

Previous work at NCSU has focused on characterization of the impact event itself (*Pearson, et al. 2007*), including quantification of the contact force between the impacting object and the composite as well as the energy dissipated by the composite, with measurements representative of the entire sample ( $10^{-1}$  m) and occurring in the  $10^{-4}$  seconds range. Other areas investigated included embedded sensor placement and density (*Garrett,*

*et al.* 2008). This work has investigated time scales of  $10^1$ - $10^2$  seconds and length scales of  $10^{-3}$ - $10^{-2}$  m.

### 1.3 Background

The principles of fiber Bragg grating strain sensors have been thoroughly documented by numerous authors and researchers (*Measures* 2001, *Othonos and Kalli* 1999). As such, this paper will not present the general background and history of these sensors. However, some explanation of unusual grating loadings and responses is useful to help explain phenomena observed later in this study. Bragg gratings are modulations in the fiber core index of refraction which produce a narrow bandwidth peak in their reflected spectrum. This peak wavelength changes linearly with applied axial strain or temperature. When the axial strain distribution along the grating is non-uniform, the reflected spectrum is distorted, as shown in Figure 1.2 (d). Secondly, when transverse compressive loading is applied to a FBG in a circular, single-mode fiber, the resulting deformed reflected spectrum has two separate resonant wavelengths due to the splitting of the original lightwave into two orthogonally polarized lightwaves with different resonance conditions (Figure 1.2, c). The separation bandwidth for these two reflective peaks is proportional to the magnitude of the transverse loading, but the bandwidth is typically less than one nanometer even in most extreme cases. In order to generate responses from a single grating that are separated much beyond one to two nanometers, another type of loading is required. Chirped gratings employ a smooth variation in the grating period, which can be either written into the fiber during manufacturing or induced by a strain gradient. These chirped gratings reflect incoming light

over a band of wavelengths instead of a single wavelength. By loading a normal grating periodically, but over a much larger period and scale than that of the original index variation modulation of the sensor, a highly separated response can be generated with the reflection of two individual wavelengths of light. The term for this grating feature is “super-structuring” and can be written into the original grating structure or, as we will demonstrate in this work, induced by strain modulations due to the periodic reinforcement placement as found in woven composites.

One widely used FBG sensing technique involves monitoring the Bragg wavelength by picking out the single wavelength with maximum response intensity. This method disregards the bulk of the grating response in order to allow measurements at high data acquisition rates. As the general strain of the grating changes, only the corresponding shift in the Bragg peak is recorded. Efforts to improve the speed of peak wavelength detection methods have resulted in several experimental systems with scanning rates of 50kHz (*Lloyd, et. al, 2004*). These systems, however, are not currently commercially available. The highest speed peak detection interrogation systems commercially available at this time are capable of achieving scan rates of 1kHz (Micron Optics sm130). Peak detection methods are limited by the distortion inherent to embedded FBG sensors. Due to damage and fabrication induced non-uniform loading along the length of the grating, as well as transverse loading, the FBG response can have several peaks which move independently and can be co-located, making interpretation of the response using peak detection alone very difficult.

Full spectrum FBG interrogation techniques provide information about the total strain state along the length of the grating. The emergence of features in the grating response that

are not captured by peak wavelength systems can thus be characterized. Current commercially available full spectrum measurement techniques are limited to acquisition rates below 5Hz however (Micron Optics si720). The low speed, full spectrum system used for this study employs a tunable cavity laser, which is unable to achieve speeds high enough to observe changes in FBG response during impact events. High speed MEMS filters, such as the one employed for the high speed, full spectrum interrogation system used in this study, allow for much higher scanning speeds.

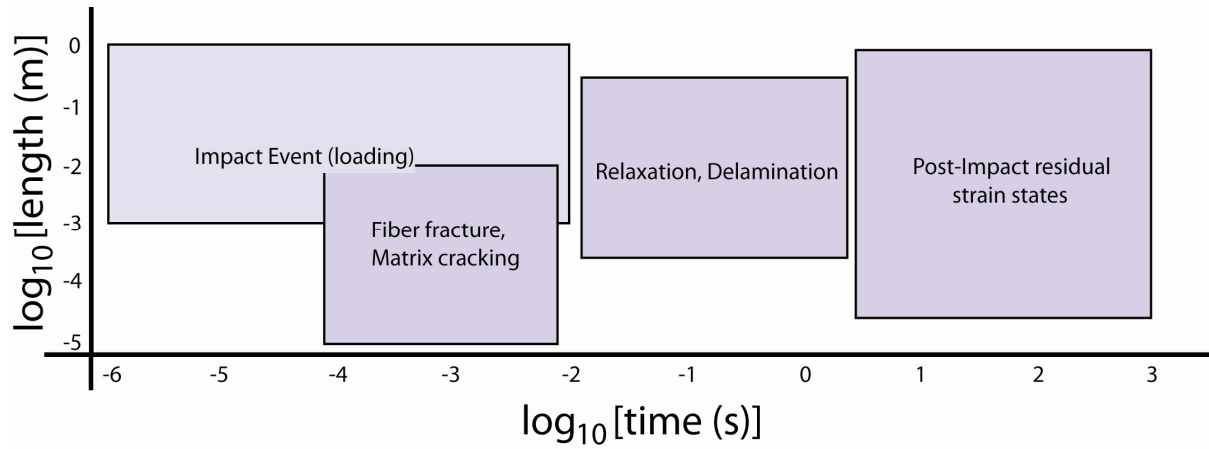


Figure 1.1. Map of spatial and temporal scales for graphite-epoxy woven composite laminate damage resulting from impacts. Time and length scale values are estimated from previous experimental data obtained at NCSU.

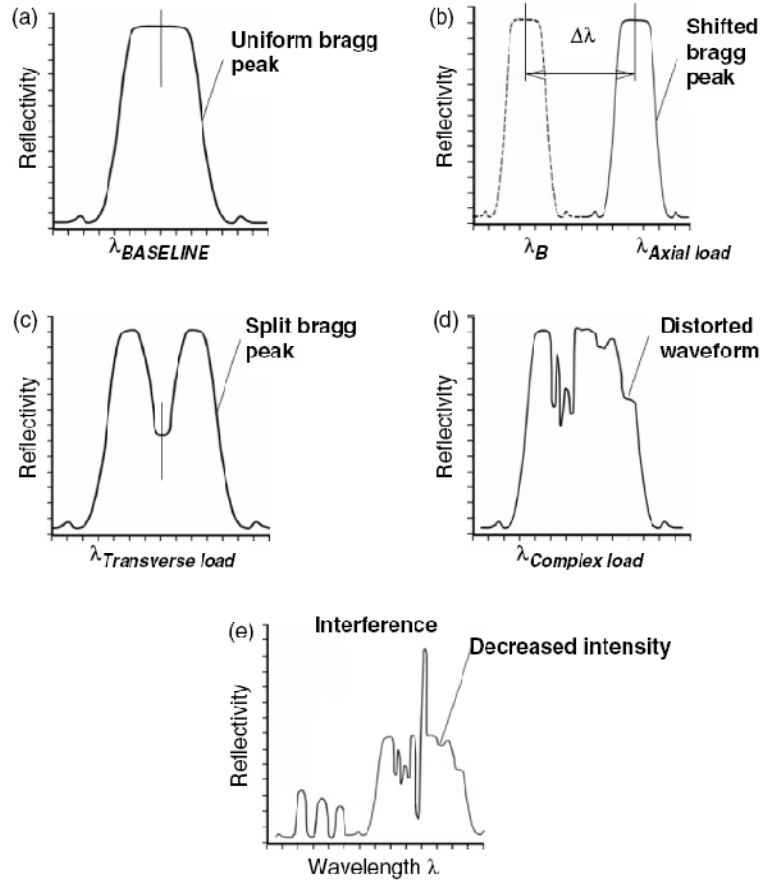


Figure 1.2. Baseline FBG response and responses due to various loading cases: (a) no load case, (b) uniform axial load, (c) transverse compressive load, (d) non-uniform applied strain field, (e) damaged sensor (Pearson, et al. 2007).

## Chapter 2. Experimental Methods

### 2.1 Sample Preparation

The samples produced for testing in this study were fabricated using a single step curing process, which included fiber embedment. In previous experiments conducted at NCSU by *Pearson et al.* (2007) and *Garrett et al.* (2008), woven carbon fiber composite specimens containing embedded optical fibers were fabricated using a multi-step process. The first step of this procedure involved fabricating the two outermost 11 layer sections of the composite. Next, the cured lamina were assembled around the embedded fiber layer with one additional lamina above and one below the fibers, creating a single 24 layer composite with fibers embedded between the 12th and 13th lamina. Survival of the sensor fibers was demonstrated, although some deformation of the fibers and signal distortion was observed. Fabrication of each sample using this method required a minimum of eight hours for the two curing cycles, plus additional time for sample preparation before and after each curing cycle.

Due to the time and complexity involved in producing specimens using this process, as well as concerns about the effect of the pressure exerted on the embedded fibers by the two pre-cured sections of the composite during the fiber embedment step, a single cure cycle procedure was devised during which a single fiber was embedded in the middle of the composite.

The single-step fabrication procedure involved assembling twelve 11.5cm x 11.5cm sheets of uncured pre-preg woven carbon fiber fabric on each side of a single FBG sensor

and curing the entire assembly in one cycle. The carbon fiber fabric used for this study used a balanced 2 x 2 twill weave and was supplied by the Advanced Composite Group. A single 2mil thickness Mylar release film and four separate pieces of polyester peel-ply fabric were used to prevent adhesion of the sample to the mold surface.

To begin the sample assembly, a single piece of Mylar approximately 30cm by 80cm was laid out on the workbench. The sheet was folded in half at the end of the assembly process to create one side of the seal during vacuuming. A 1.5cm diameter snake of plumber's putty was placed on three edges of the Mylar to form the seal for the three remaining sides with some additional putty placed at both ends of the snake where the Mylar is to be folded in half. Two 10cm x 16cm peel-ply pieces were placed in the center of the putty ring overlapping one another to create a 16cm square. The lower 12 lamina were removed from their plastic and wax paper backing and stacked in place in the center of the peel-ply square aligned with one another. The sensor fiber was then placed on top of the lower layers at 0° orientation to the carbon fabric and 12.5mm offset from the center of the sample, with the center of the Bragg grating centered. To maintain sensor alignment, the ends of the fiber were taped to the workbench, holding the fiber taut. The remaining 12 layers of pre-preg were then assembled on top of the lower layers and sensor fiber. To provide protection for the fiber from excess epoxy resin during the curing process, a small ball of plumber's putty was placed around the fiber on either side of the sample. The ends of the sensor fiber were then allowed to exit the Mylar by passing through a ring of putty and the assembly was vacuumed to remove as many air voids as possible between the layers of the sample. Once sealed, the assembly was then moved to the hot press and placed between two

flat steel plates for the duration of the curing cycle. Following the curing cycle, the assembly was removed from the press and disassembled in reverse order. Figure 2.1 shows a partially assembled sample ready to receive the final layers of peel-ply and Mylar in preparation for application of a vacuum. In Figure 2.2, a schematic cross section of a fully assembled sample is shown, while Figure 2.3 shows the placement of the FBG within the sample.

By using two overlapping pieces, the peel-ply could be peeled off from the center of the sample at a low angle out towards the edge of the sample, preventing excess resin from breaking and preserving the sensor fiber. Once free of the peel-ply, the excess epoxy was carefully broken off manually without affecting the embedded fiber. A completed sample with most of the excess epoxy removed is shown in Figure 2.4.

Initial samples were cured in a hot-press using a stepped temperature profile ranging from 50-80°C and a constant pressure of 690kPa. The temperature profile consisted of 15 minutes at 50°C, 15 minutes at 65°C, and 180 minutes at 80°C, followed by 30 minutes with the heating elements off, allowing the sample to cool. After the four hour curing cycle, the sample was removed from hot-press and allowed to continue cooling to room temperature. Previous samples fabricated by *Garrett et al.* (2008) had been produced at twice this pressure, but embedded fibers close to the impact failed well before the composite failed. Samples produced by the current technique proved to survive a higher number of impact events prior to penetration as compared to the samples produced using the two step method and demonstrated the same failure modes. These results indicate that the lower pressure used during fabrication did not affect the integrity of the composite while providing better survivability and lower signal losses for the embedded optical fiber.

Another key difference from previous work involved the use of polyimide coated optical fibers. *Garrett et al. (2008)* demonstrated that acrylate coated fibers close to the point of impact were particularly susceptible to premature failure. Also, it was shown that fibers placed further away from the point of impact had very little response to accumulated damage to the composite, thereby making the sensor and location of little value for determining the health of the structure. Due to the greater toughness of the polyimide fibers when compared to the acrylate fibers used previously (*Carmen and Sendeckji 1995*), sensors could be located closer to the point of impact and survive for a greater percentage of the life of the sample while yielding much more useful information about the health of the composite. Other benefits include a greater likelihood of the sensor surviving the manufacturing and handling processes, which is desirable for real-world implementations of embedded fiber Bragg grating sensor based sensing systems.

In total, 18 samples were produced using the described fabrication technique. Seven samples were produced with no embedded fibers and 11 with embedded FBG's (listed in Table 2.1).

## **2.2 Impact Testing**

To provide consistent and controlled low-velocity impacts, North Carolina State University's drop tower facility was utilized. The tower, which is shown in Figure 2.5, consists of a 19mm diameter hemispherical steel impacting probe on a 5.5kg aluminum crosshead. Specimens are mounted between two 76mm diameter steel clamping rings with a layer of 1.5mm neoprene film on each side to distribute clamping pressure evenly over the

clamped area of the sample. The drop tower was used to subject composite specimens to impact velocities of 2.0-2.25m/s, yielding energies of 11.0-13.9J. A piezoelectric accelerometer and a magneto-restrictive position sensor integrated into the crosshead were used to determine the response of the crosshead to the impact with the composite specimen. These measurements provide the velocity of the crosshead both pre- and post-impact to determine the amount of energy dissipated by the sample as well as the contact forces and surface deflections involved.

Each impact event was initiated by manually raising and aligning the crosshead with marks corresponding to specific impact energies. During the rebound following impact with the specimen, the crosshead was manually arrested to prevent secondary strikes. Failure was defined as complete perforation of the sample with no rebound of the crosshead.

During the final strikes near failure, the rebound velocity was very low, with much of the energy dissipated by the sample. In a small number of strikes, this resulted in a low energy secondary strike as it was not possible to fully arrest the crosshead before it contacted the sample again. These secondary strikes are not regarded as significant to this study as the majority of the impactor energy had already dissipated when they occurred.

Before each strike, the voltage reading with the impactor resting on the surface of the sample was measured, and the trigger voltage set to 20mV above this reading, corresponding to a point approximately 4.6mm above the specimen surface. Once the position sensor returned a voltage below this trigger voltage, the oscilloscope began recording 1002 data points at a rate of 50kHz for both position and acceleration. This moving trigger point prevented errors in the post-processing of the oscilloscope data for the calculation of

dissipated energy, as the averaging of pre- and post-impact velocities depended upon the time window applied.

### **2.3 FBG Sensor Interrogation**

Three different FBG interrogation techniques were employed for this study. Low speed, full spectrum data was captured at 0.1Hz. High speed peak wavelength detection was employed at 1.0kHz. Finally, high speed, full spectrum data was gathered at 200-926Hz. The results of these interrogation techniques was then compared with the previously described impact characterization data.

#### **2.3.1 Low speed, full-spectrum**

Some FBG sensors were interrogated in transmission using a Photonetics tunable laser source in conjunction with a photo-detector to scan across the spectral band containing the FBG response spectrum. The laser provided a narrow bandwidth light source which was routed into one end of the embedded fiber. After passing through the embedded sensor, the intensity of the transmitted light at that wavelength was measured with a photo-detector. This interrogation technique was performed for spectral scans over a 2-3nm bandwidth with a resolution of 5pm, controlled by a LabView program. Scans were conducted approximately 60-90 seconds after each strike and required 90-120 seconds to complete. Because of the slow speed of this interrogation technique, no useful data could be recorded during the actual impact event, therefore post-impact residual strain states were measured using the tunable laser following each strike.

### **2.3.2 High speed, peak wavelength detection**

Some FBG sensors were interrogated in reflection during the actual impact events by a Micron Optics SM130 high-frequency scanner providing peak Bragg wavelength detection at approximately 1.0kHz (Figure 2.6). One to two seconds of data were recorded before each impact event, with recording continuing both throughout the strike and for an additional two to three seconds following the strike event. This provided a value of the Bragg wavelength before and after the event as well as the transient shift occurring within the timeframe of the contact between the impact head and the surface of the composite. The duration of the impact events were 5-10ms; therefore approximately 5-10 data points were collected during the actual event.

### **2.3.3 High speed, full-spectrum**

A third FBG interrogation system was employed for this study through collaboration with Dr. Richard Selfridge and Dr. Steve Schultz of the Department of Electrical Engineering at Brigham Young University (BYU). This research prototype interrogation system is similar to a previous system developed at BYU called the fiber sensor integrated monitor (FSIM) (Figure 2.7). It utilizes a super-luminescent light emitting diode (SLED) source in conjunction with a tunable MEMS based tunable optical filter to provide a narrow bandwidth source that can be rapidly scanned through a wide range of wavelengths (*Lloyd et al. 2007*). After passing through the filter, the signal is sent to both a reference FBG and to the sensor FBG. The reference grating is included to provide a calibration point for the measurement grating, as the wavelength transmitted by the filter can shift over time due to heating and

other effects. After being reflected by the gratings, the reflected intensities are then combined and converted to an electronic signal by a photo-detector (*Kunzler et al. 2009*).

At the time of this study, the BYU instrumentation recorded data at approximately 0.8 M samples/second. Although the MEMS filter and data acquisition electronics were capable of operating much faster, with filter scanning speeds of up to 100kHz over up to 15nm and data acquisition at up to 25 M samples/second at 12 bit resolution, the current speed is limited by the data processing and communication systems (*Kunzler et al. 2009*). An inverse relationship exists between the bandwidth being scanned and the frequency at which it can be scanned. For this reason, when capturing both the reference sensor and the embedded sensor, which requires a bandwidth of at least eight nanometers to allow room for applied strain, the maximum scanning rate is slower than when only scanning over the band around the embedded sensor, which only requires three nm of bandwidth. For the first two samples tested, the “window” was kept constant with both the embedded and reference sensors covered by the frequency sweep. For the final two samples, the window was adjusted to fully capture the embedded signal only in an effort to maximize the scanning rate, although at the expense of the reference grating.

To improve the signal to noise ratio, an erbium-doped fiber amplifier (EDFA) was applied to increase the incoming light-wave intensity before it entered the embedded fiber. For the last two samples, the EDFA power was adjusted between strikes in an effort to provide the highest possible signal-to-noise ratio for the embedded FBG as signal attenuation fluctuated across the life of the sample. As will be seen in the following chapter, during some strikes, the signal attenuation decreased dramatically, causing the post-strike signal

response to saturate the photo-detector, preventing the grating response from being completely characterized immediately following the strike. Also, when the signal was highly attenuated, the power could not be increased sufficiently to generate a grating response near saturation for fear of damaging the optical connectors or other system components.

For all samples tested using BYU's instrumentation, the reference grating Bragg wavelength was 1544.18nm. The nominal Bragg wavelengths for all embedded sensors in all tests before embedment were centered at 1550.00nm. This allowed the embedded sensor spectrum to shift over five nanometers in compression before overlapping the reference grating signal.

The output of this interrogation system was buffered in memory and then saved in files containing approximately 3 million data points each. The data was stored in binary with an ASCII header preceding each wavelength sweep which included information such as the timestamp, scan number, number of points in the scan, and the starting position of the scan. The impact events were manually synchronized with the data storage such that the impact event did not occur at the transition from one data file to the next.

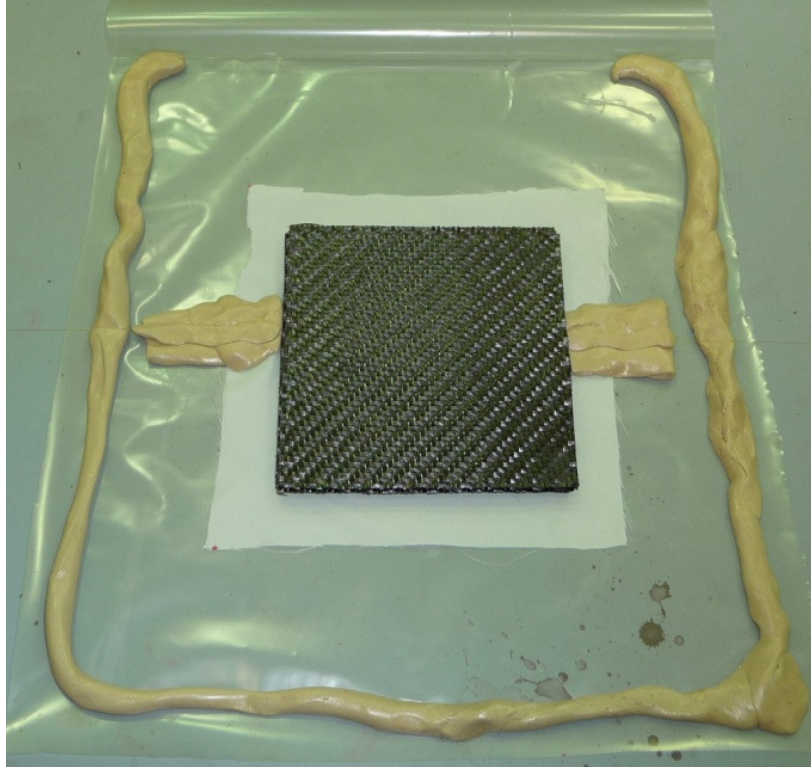


Figure 2.1. Embedded fiber specimen prior to curing cycle with Mylar release film, peel ply, and putty in place and ready to receive upper peel-ply layers, and vacuum tubing before sealing and applying vacuum.

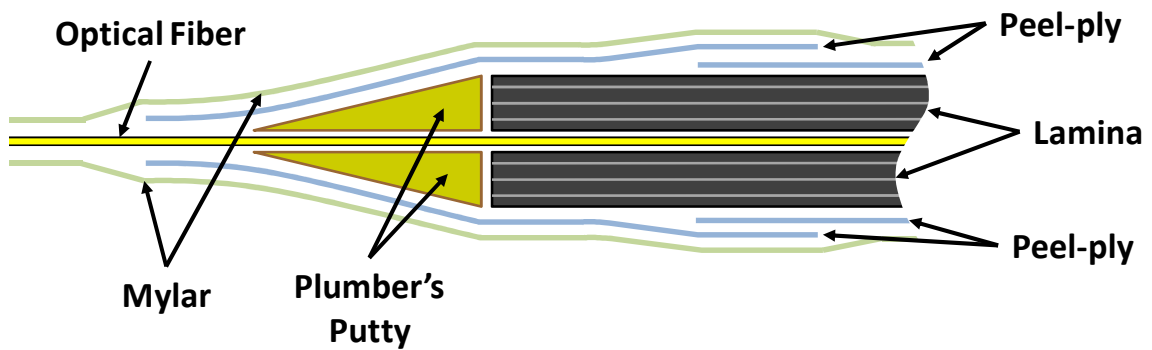
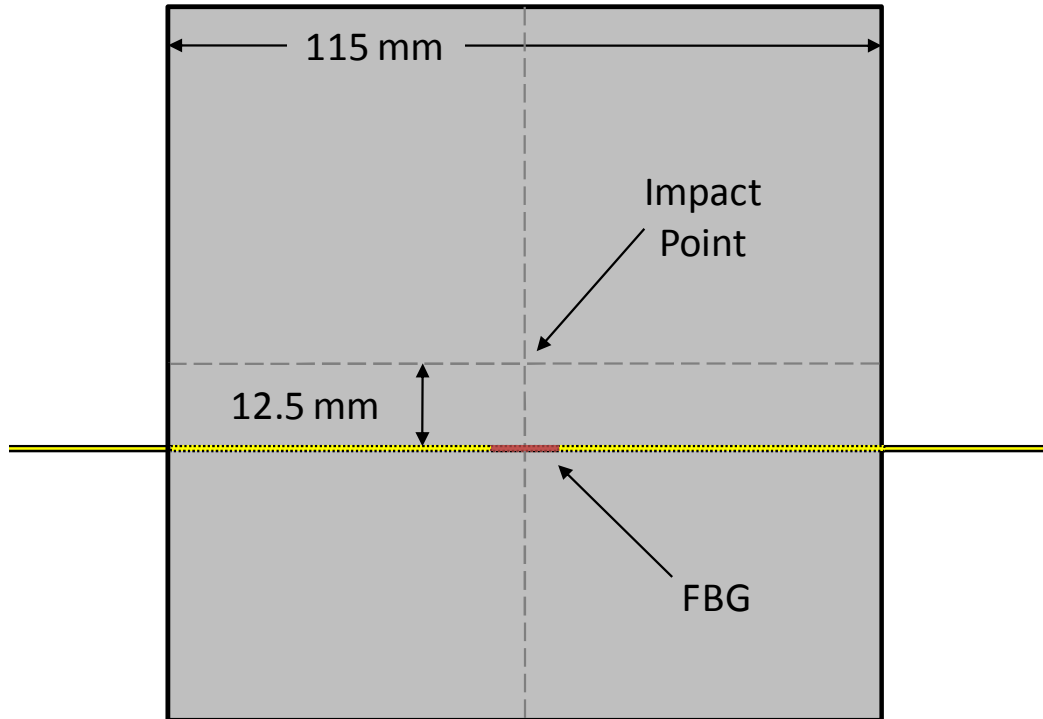


Figure 2.2. Cross section of specimen layup at embedded optical fiber showing overlapping peel-ply, protective putty, fiber, lamina, and outer mylar layers (not to scale).



**Figure 2.3. Layout and dimensions of specimen with embedded Fiber Bragg Grating.**



**Figure 2.4. Composite specimen with fabrication materials and excess epoxy removed and ready to be installed in the impact tower.**

**Table 2.1. Samples produced for this testing with embedded fiber Bragg gratings and their specifications.**

Sample Number	S-1	S-2	S-3	S-4	S-5	S-6	S-7	BY-1	BY-2	BY-3	BY-4
Input Strike Velocity	2.00	2.00	2.00	2.00	2.00	2.00	2.00	2.00	2.13	2.25	2.13
Dissipated Energy Per Strike (J)	11.0	11.0	11.0	11.0	11.0	11.0	11.0	11.0	12.4	13.9	12.4
Strikes to Failure	49	7	24	79	30	175	68	31	82	12	49
Distance from Point of Impact to FBG (in)	0.50	0.50	0.50	0.50	0.50	0.50	0.50	0.50	0.63	0.50	0.50
Low Speed, Full Spectrum	No	Yes	Yes	Yes	Yes	Yes	Yes	No	No	No	No
High Speed, Peak Wavelength	Yes	Yes	Yes	Yes	Yes	Yes	No	No	No	No	No
High Speed, Full Spectrum	No	Yes	Yes	Yes	Yes						
High Speed Full Spectral Scan Rate (Hz)	n/a	200	534	926	Variable						

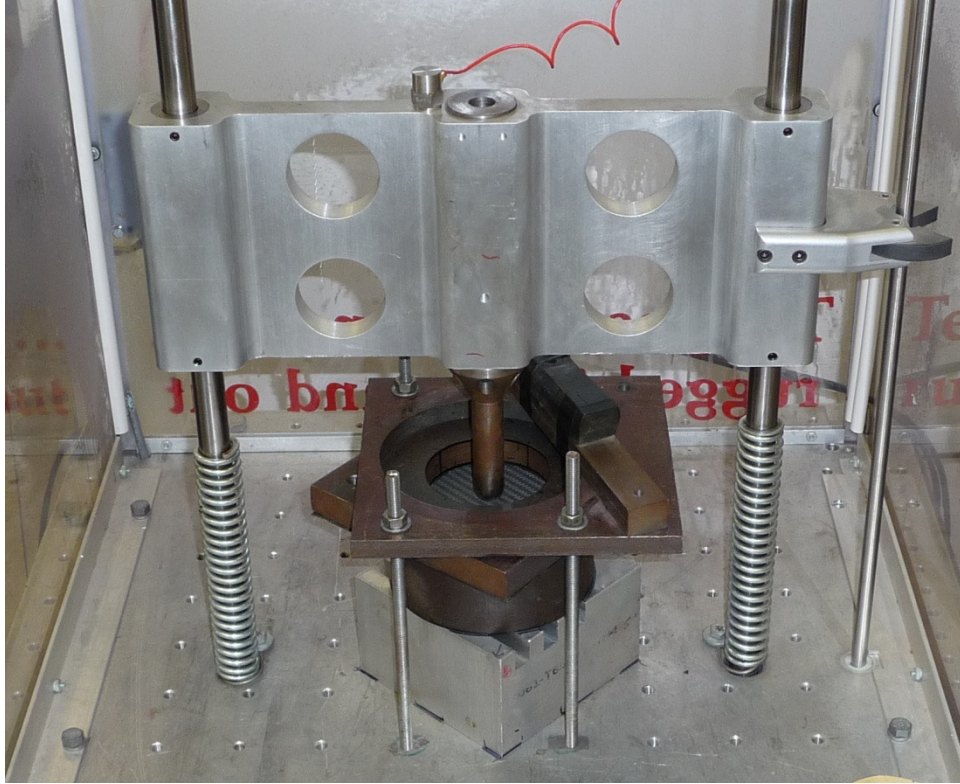


Figure 2.5. Specimen with embedded FBG sensor mounted in instrumented drop tower.

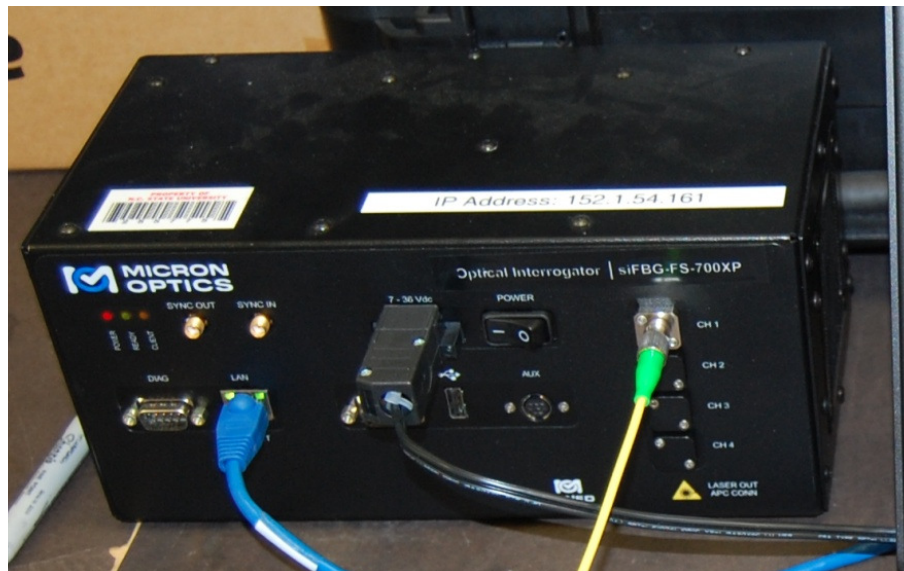


Figure 2.6. Micron Optics SM130 high speed peak-detecting optical interrogator.

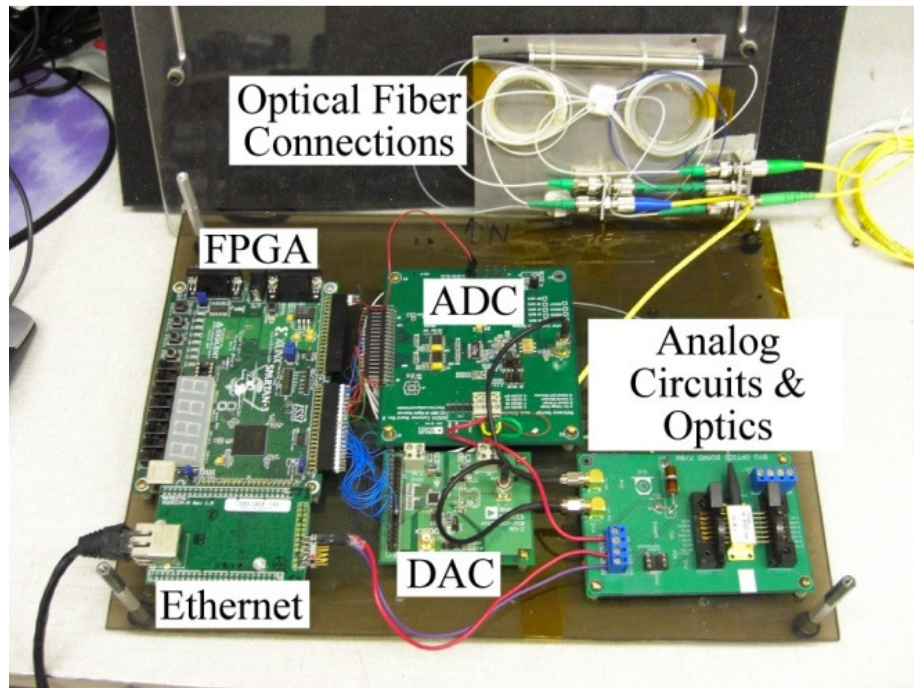


Figure 2.7. FSIM high speed full spectrum optical interrogator developed at BYU.

## Chapter 3. Experimental Results and Analysis

### 3.1 Low speed, full spectrum data

In previous work at NCSU by *Garrett et al.* (2008), emphasis was placed on full spectral characterization of the quasi-static embedded grating response in between damage events. Work by *Pearson et al.* (2007) had provided a description of the impact event itself by outfitting the impactor with acceleration and position sensors and monitoring its behavior during the short duration damage event. *Garrett et al.* (2008) showed the relative relationship of FBG longevity and sensitivity to the proximity of the embedded FBG to the point of impact. Due to the number of optical fibers embedded, the sensors affected the global performance of the composite. Additionally, the two-step composite fabrication process and crossed multi-layer optical fiber layout resulted in a shorter FBG lifespan due to the additional stress at points where fibers crossed. With a single grating embedded 0.5 inches from the impact point and a single step fabrication procedure, sensor survivability was improved.

Since the scan rate of the tunable laser is far too slow to observe any transient events during damage events, the post-impact residual strain state was interrogated in between each strike to observe changes in the shape and intensity of the FBG spectral response. Seven different specimens were interrogated with the slow speed, full-spectral scans, as listed in Table 2.1. Figure 3.1 shows a typical grating response for an undamaged composite and for one that has been subjected to several impacts. Features of note as damaged was induced are

the decrease in reflected signal amplitude, the shift away from the original Bragg wavelength (1550.0nm for this sensor), and the broadening and splitting of the main Bragg peak. Since these features have been well documented in previous work, this study will not focus on them. It should be noted that while the undamaged response shown in Figure 3.1 appears very similar to the ideal Bragg grating response, in fact, many of the embedded gratings exhibit some level of moderate distortion and Bragg wavelength shift as a result of strains imparted in the composite fabrication process.

Although several sensors were lost prematurely, others survived until failure of the composite. The fiber failed in sample S-4 after 30 strikes, while the composite failed after 79 strikes. Figure 3.2 shows the low speed full spectral scans for this sensor, wherein each scan has been represented as a single line across the image with relative signal intensity represented by the color along the line. Damage and time progress from the top of the image down towards the bottom. Clearly, the FBG response can be seen shifting from its original center around 1550.8nm to a lower wavelength after the first strike. Following the subsequent strikes, the general progression was towards higher wavelengths, along with a steady attenuation of the signal intensity. By strike 06, there are clearly two separate Bragg peaks, which remain until the response was too broad and highly attenuated to see. Throughout the testing, the bandwidth over which the laser source was scanned was adjusted in an effort to fully capture the grating response. In Figure 3.3, the impact characterization data, and in particular the maximum contact force data, shows a similar progression as that of previous specimens in *Pearson et al.* (2007) and *Garrett et al.* (2008). One exception is that the dissipated energy did not rapidly increase with strike number towards the end of the

composite lifetime, as previously observed. This may have been due to the change in fabrication process implemented in this work. This observation is also consistent with the fact that the FBG sensor spectrum did not rapidly change prior to failure of the sensor, but rather slowly attenuated with strike number.

Low speed full spectrum data sets for samples S-6 and S-7 are shown in Figure 3.4 and Figure 3.6 respectively, with their corresponding impact characterization data shown in Figure 3.5 and Figure 3.7. With sample S-6, both the embedded grating and impact characterization data show an unusual shift in behavior around strikes 10 and 92. This behavior appears as a sudden wavelength shift in the FBG reflected spectrum and a sudden decrease in the maximum contact force at strike 10 and a sudden decrease at strike 92. The dissipated energy also demonstrated a sudden decrease at strike 92. This behavior in the contact force has not been observed before, however it is not due to the instrumentation as the changes appear in both the FBG sensor and impactor data sets, which are measured and captured completely separate from each other. As the effect in the global parameters was significant, these signals are most likely indicative of delamination within the laminate. With sample S-7, noticeable features in the FBG sensor data are the sudden shifts in signal shape and intensity at strikes 25 and 30, as well as the significant amount of peak splitting throughout the lifetime of the composite. No obvious feature in the impact characterization data, which are similar to those previously observed in *Pearson et al.* (2007), can be correlated to these shifts. This indicates the primary failure mechanisms were primarily localized in this specimen.

### **3.2 High speed, peak wavelength data**

Using the Micron Optics SM30 high speed peak detecting interrogator, peak wavelength data was gathered at approximately 1kHz for Specimens S-1 through S-6. In Figure 3.8, a typical response from Specimen S-1 is shown in which 12 data points were recorded during the transient strike response, showing a rapid shift in peak wavelength to a minimum value from the pre-strike steady state wavelength, and a corresponding shift back to a new steady-state wavelength. As this particular data was recorded during an impact later in the life of the composite (strike 36 out of 49), the duration of the impact event had increased substantially over the duration for early impact events.

In Figure 3.9, the peak wavelength data over the lifespan of Specimen S-1 is shown. The steady-state Bragg wavelength before and after the impact events are plotted, along with the Bragg wavelength recorded at the point of maximum shift during the strike event. The steady-state values do not provide much of any information about the damage event that occurred between them. However, the transient peak wavelength value seems to correspond to the impact characterization data for S-1 (Figure 3.10). Around strike 30, the rate of decrease of the contact force and the rate of increase in the dissipated energy both change. In the peak wavelength data, the magnitude of the transient shift can be seen to begin decreasing beyond this strike.

One of the limitations of the fast scan peak wavelength data relates to the distortion of the embedded sensor response due to damage. As shown in the low speed full spectrum data of Figure 3.2, broadening and attenuation of the main peak are common. At several points during the lifespan of many specimens, the scanner erroneously indicated that multiple Bragg

peaks were present, highlighting one of the drawbacks of using peak-detection only for damage detection with embedded sensors. These additional peaks were the result of spectral broadening and distortion due to damage induced deformation of the FBG. Additionally, when the Bragg wavelength jumped during strike events, the instrumentation sometimes lost the location of the peak. Only after the large transient movement had subsided would the peak-detection software relocate the sensor wavelength. These changes in the embedded grating response make interpretation of peak wavelength data alone very difficult. A second limitation is the limited number of data points during each impact event. As seen in Figure 3.8, the maximum peak wavelength has to be estimated from the data points and can be highly sensitive to when these points are acquired relative to the start of the impact event. This was particularly important for strikes early in the lifetime of the laminate, for which the impact response of the laminate occurred over a small timescale.

These results demonstrate the advantages and challenges of using peak wavelength data from embedded FBG sensors for damage identification. From Figure 3.9 we do not see a significant change in the post-impact wavelength measurement throughout the lifetime of the composite. On the other hand, the maximum wavelength shift measured during the impact event (provided the above issues could be resolved by faster interrogation systems with multiple peak detection capabilities) could provide critical information. While peak wavelength data is easier to collect than full-spectral data, we will see in the following section that it does provide the same density of information about the damage formation within the laminate.

### **3.3 High speed, full spectrum data**

Four specimens were tested while interrogating the FBG sensors with the FSIM high speed, full spectrum instrumentation. Table 3.1 lists the key parameters for the four samples tested. Since this interrogation technique had not been attempted with embedded FBGs in composites, the test parameters such as the spectral scan rate, the distance between the impact and FBG, and the energy input per strike were varied in order to obtain a broad range of data.

Sample BY-1 was the first sample tested with the high-speed full-spectrum equipment. During transport to NCSU, BYU's EDFA was damaged and could not be used to boost the signal intensity for any samples. Samples BY-2, BY-3, and BY-4 were later tested using an EDFA to amplify the input signal.

Data collected during the testing of sample BY-1 was recorded using NCSU's analog-to-digital converter, wherein the BYU photo-detector output was stored as a continuous stream of intensity information. The data stream was broken into individual frequency sweeps and stored using a MATLAB script (Appendix B). Figure 3.11 shows a representative section of a data set. A single complete frequency sweep is shown, along with portions of the preceding and following frequency sweeps. The responses of the reference grating and the embedded grating are clearly visible as the MEMS filter sweeps from approximately 1530nm to 1560nm. The FBG responses are also visible between the frequency sweeps as the filter rapidly resets to begin the next sweep (labeled the flyback response). In order to break the data into a set of individual frequency sweeps, the reference grating response was identified by scanning the data stream for regions where multiple data

points averaged above a set trigger value. This value was set to be higher than the maximum intensity value of the embedded FBG but lower than the maximum of the reference FBG. The data was filtered using a ten point averaging window to prevent false triggering on the grating responses in the filter fly-back and to remove uncharacteristic spikes in the intensity, allowing for more consistent results (see Figure 3.12). The filter window covers a wavelength bandwidth of approximately 48pm.

Once the reference grating response was found, a window of 4000 data points containing both the reference and embedded grating responses was stored as a single row in a matrix, with subsequent data windows stored in ensuing rows. To display this new data set, the matrix was displayed as an image with color values set based upon the intensity values. A full data set is shown in Figure 3.13, with the axes adjusted to show time in milliseconds relative to the estimated impact start time and the wavelength shift from the original Bragg wavelength in nanometers. The color range has been adjusted to correspond to the maximum and minimum values of the embedded FBG, causing the reference sensor saturate. A close-up image of the embedded sensor response was used to better observe the transient response during the impact itself and immediately following (Figure 3.14).

For samples BY-2 through BY-4, NCSU's analog-to-digital converter was not used. Instead, the data was directly stored by BYU's FSIM system. As such, each frequency sweep was already individually stored. Figure 3.15 shows a single frequency sweep from sample BY-2, containing the saturated reference grating and the embedded signal. The reference grating response is saturated due to the use of an EDFA to improve the intensity of the embedded sensor response and the related signal-to-noise ratio. The sweeps were filtered

using a five point averaging window filter to remove the remaining high frequency noise. The filter window corresponded to a wavelength bandwidth of approximately 38pm. The dataset was processed by removing the ASCII header between the individual frequency sweeps and storing the sweep data in a matrix in a similar manner to BY-1. Figure 3.16 and Figure 3.17 show a full data set and close-up view of the impact response from BY-2 strike 01. Due to the higher scanning rate for BY-2, the time-domain resolution is clearly improved over that of BY-1.

### **3.3.2 Sample BY-1**

Sample BY-1 was the first sample to be impact tested using BYU's FSIM instrumentation to interrogate the embedded FBG, which was scanned at 200Hz. The sample exhibited a typical response compared to other samples test, with failure occurring on the 31<sup>st</sup> impact. The embedded sensor was interrogated with the unamplified output from the MEMS filter. The bandwidth over which the filter scanned was held constant throughout all strikes, resulting in a constant frequency sweep rate. The general progression of the response consisted of increasing contact duration, along with gradual attenuation of the sensor response and increased distortion and broadening, with a sudden re-intensification halfway through the life of the sample.

Strikes 6 through 11 showed only short duration transient events occurring in a single scan with a narrow, well defined main peak and a much weaker secondary peak.<sup>1</sup> In strikes 6-8, a transient tensile strain is indicated by the shift towards higher wavelengths (Figure 3.18), while in strikes 9-11, very little can be observed during the impact as the response is

highly attenuated or not visible in any scans (Figure 3.19). The only indications of the impact event are the sudden shifts in the quasi-static response or single scans with no apparent response. This type of fast, clean response is expected as the composite continued to retain much of its strength with damage occurring in the form of rapid fiber breakage and matrix cracking.

While initially at a relatively high intensity, the FBG signal weakened and broadened continually from strike 6 until strike 15 (Figure 3.20).<sup>1</sup> Fractures in the composite stretching out from the point of impact along the direction of the reinforcement, which intersected the position of the embedded FBG, could cause localized micro-bending and transverse loading of the grating, resulting in this type of response. Following strike 15, the sensor response suddenly regained intensity and narrowed to a single main peak (Figure 3.21). This re-intensification likely resulted from sudden delamination in the lamina surrounding the sensor, releasing the accumulated strain concentrations on the FBG sensors. While some further distortion and broadening occurred later in the life of the sample, the high levels of attenuation observed prior to strike 15 did not reappear.

Following strike 11, a weak response appeared at a wavelength 4nm longer than the main response. This feature persisted through at least strike 15 and experienced shifts due to the strike events, with a separation of approximately 5.5nm from the main FBG response following strike 14, as shown in Figure 3.22. This feature is likely the result of periodic “super-structuring” of in the grating, wherein a regular change in period of the grating occurs over a length scale much greater than that index period written into the grating during

---

<sup>1</sup> Data sets for BY-1 strikes 1-5, 16-18 were overwritten and are not available for analysis.

manufacturing. Due to the woven nature of the reinforcement used in the composite, the necessary conditions for periodic load distribution along the length of the sensor are easily possible.

During strikes 13, 19, 26, 29, and 30, the intensity of the transient response during the strike event was significantly higher than that of the grating response preceding and following the impact (Figure 3.23). Contrastingly, the intensity of part of transient responses during strikes 10, 11, 15, 20, 22, 25, and 29 is nearly too low to observe (Figure 3.21). These drastic changes could be attributed to unloading of the fiber away from the FBG. As the energy wave created by the impact propagates outward in the sample, interaction between the composite sample and the impact tower mount may cause a sudden change in clamping pressure at the position of the fiber.

From strike 19 until failure, smooth relaxation from compression to tension is readily apparent (Figure 3.24) in the FBG sensor response immediately after the start of the impact. Initially, the relaxation is very low in magnitude and duration. As the sample nears failure, however, both the magnitude and duration of the relaxation response increases. This trend has also been observed for the duration of contact between the indenter and the specimen and is an indication of a transfer of energy dissipation from fiber breakage and matrix cracking (occurring at extremely rapid time scales) to the mechanisms of delamination and matrix deformations (Pearson, et. al, 2007). This increase in contact duration has been previously proposed as a measure of the damage state within a specimen due to the increased compliance of the specimen through large permanent deformations near the regions of damage propagation (*Yigit and Christoforou 1994; de Morais et. al 2005*). These results

demonstrate that this measure could equally be applied to the relaxation response time of the laminate itself, a far more direct measure of the material compliance.

The impact characterization data for sample BY-1 is shown in Figure 3.25. The point of “critical damage” occurs around strike 21. No systemic change in the high speed full spectrum data is apparent around or following this strike.

### **3.3.1 Sample BY-2**

Sample BY-2 exhibited the slowest change in response of all the samples tested with the FSIM instrumentation. The response exhibited gradual changes from strike to strike, with very few substantial variations, which is likely due to the increased distance from the point of impact to the embedded sensor. Failure of the sample occurred on the 82<sup>nd</sup> impact. The spectral bandwidth scanned by the MEMS filter was held fixed throughout the life of the sample and encompassed both the reference grating and embedded grating responses. The resulting scanning rate was 534Hz, which is just over two and a half times the scanning rate for sample BY-1. The intensity of the response was boosted by using an EDFA to amplify the filter output. The amplification power was set before beginning the testing such that the embedded FBG response nearly saturated the photo-detector in anticipation of subsequent attenuation of the response. This provided a much improved signal-to-noise ratio over the background noise.

Similar to sample BY-1, the general progression of the response consisted of slowly increasing numbers of wavelength scans during the actual strike, along with slow attenuation of the intensity of the sensor response and increasing distortion and broadening. Through the

early life of the sample, the transient sensor response during the strikes showed general shifts in the grating response toward shorter wavelengths, or compression, with no indications of matrix relaxation following the strike itself. The magnitude of the compression response quickly decreased as damage progressed and a tension response became dominant. In the later strikes the spectra split into two peaks, and in the final series of strikes, post-strike matrix relaxation became a significant feature of the response.

During the first five strikes, the transient strike event occurred very quickly. Figure 3.26 shows a typical response, in which only two spectral scans were captured during the strike with the next scan exhibiting the non-transient response repeated thereafter. These strikes exhibited a clean compression response. In strikes 15 through 28, the compression response is no longer readily apparent, with only an attenuated tension response (Figure 3.27), although not all strikes exhibit either one. While the pre- and post-strike spectra do not show signs of a split peak, the spectra during the strike began to have multiple weak peaks.

Beginning with strike 29, it is observed that the quasi-static response has split into two separate peaks (Figure 3.28). Also in this strike, the response during the impact is highly attenuated through the initial scans, with a single scan at the end containing an intense peak. The subsequent scan contains the same grating response and reduced intensity as the remaining scans in the data set for the strike. These features are found to some degree in many of the strikes up until failure. Once again, it should be noted that the sudden increase in intensity at the end of the strike could be attributed to unloading of the fiber away from the FBG.

Two separate peaks with equal intensities develop from strike 53 through strike 65 (Figure 3.29). This type of response is generally indicative of a transverse load through the cross section of the grating. Following strike 66, the higher wavelength peak begins to diminish, leaving the compression peak as the only peak.

Beginning with strike 67 until failure, relaxation from tension towards compression immediately following the strike becomes apparent (Figure 3.30), which is exactly opposite from the response observed with sample BY-1. As the sample nears failure, the magnitude and duration of the relaxation response increases significantly. By strike 81, the last strike before the strike causing failure, the relaxation is the dominant feature in the FBG response.

Throughout the life of the sample, several strikes contained an unusual feature in which the transient grating response exhibited an oscillation rather than the simple shift and return as was seen in the majority of the strikes. These events generally took longer to occur than the typical response. Figure 3.31 and Figure 3.32 show these events, which occurred in strikes 6, 15, 39, 42, 53, 61, 64, 68, and 77. This behavior might be attributed to the final failure of a stiffer section of the composite, followed by the subsequent widespread failure through the matrix or delamination of a weaker section. This behavior does not seem to have any correlation with the impact characterization data obtained over the life of the sample (Figure 3.33).

The impact characterization data does show some correlation between the point of “critical damage,” where the contact force and dissipated energy per strike begin to drop and increase respectively from their plateaus. This change occurs around strike 70, which correlates well with the appearance of matrix relaxation in strike 67 (Figure 3.30).

### 3.3.3 Sample BY-3

Sample BY-3 was impacted with higher energy per strike (13.3J) in order to reduce the number of strikes required to reach failure. The increased energy imparted, in combination with the natural variability of the composite specimens, lead to an extremely reduced lifespan, with the sample failing after only 12 strikes. Before each strike, the EDFA power setting was adjusted to provide the strongest signal-to-noise ratio possible for the embedded FBG. Before testing began, the bandwidth scanned by the MEMS filter was set to completely cover the expected response range of the embedded grating (1547.8–1552.2nm) but not the reference FBG. This was done in order to improved the scanning rate and thereby improve the resolution of the transient strike response. This 3nm window was held constant throughout the life of the sample in order to keep the scanning rate consistent (926Hz).

Similar to the previous sample, the response consisted of rapidly increasing numbers of wavelength scans during the actual strike. The increased scanning rate is apparent in strike 02 (Figure 3.34), with the transient response appearing in four individual sweeps, as opposed to the initial strikes for sample BY-1 and BY-2 in which at most a single scan captured a transient response during the early strikes. Although the signal strength was adjusted before each strike, general attenuation of the intensity of the sensor response and increasing distortion and broadening occurred. Due to this attenuation, by strike 09 the EDFA power had been set just below 1.0W. For the remaining strikes, the EDFA power could not be increased further to prevent damage of the FSIM interrogator and optical fiber connectors.

As with the previous samples, the transient sensor response during the initial strikes showed general shifts in the grating response toward shorter wavelengths (Figure 3.34), with no indications of matrix relaxation following the strike itself. The magnitude of the compression response quickly decreased as damage rapidly progressed (Figure 3.35). In most of the later strikes, a clear tension response is observed towards the end of the impact event, although a rapid compression response is still observed during several strikes in the first frequency sweep, as shown in Figure 3.36 and Figure 3.37. In the last three strikes, post-strike matrix relaxation became somewhat of a significant feature of the response, although to a much lesser degree than in the previous samples (Figure 3.38).

Following strike 06 the spectra split into numerous peaks and remained this way until strike 09, where the response recombined into two highly attenuated peaks. Due to this sudden change, between strikes 09 and 10, the scanning bandwidth was temporarily increased to capture both the embedded and reference sensors. In Figure 3.39, this additional data clearly shows several additional spectral peaks at wavelengths 2.0, 2.8, and 3.5nm shorter than the main embedded sensor response. This response is once again attributed to a super-structuring of the grating. Although the remaining strikes showed increases in intensity of the main peak, the response following strike 11 shows a highly attenuated and diffuse peak nearly 1.5nm away from the main response (Figure 3.37) which is likely resultant from the same super-structuring.

The impact characterization data for sample BY-3 is shown in Figure 3.40. Very little can be inferred from this data and the high speed full spectrum data due to the extremely short lifespan of the sample.

### 3.3.4 Sample BY-4

Sample BY-4 was the last sample tested to date using the FSIM instrumentation. Due to the short lifespan of sample BY-3, the impact energy per strike was reduced to 12.4J. As with sample BY-3, the EDFA power setting was adjusted before each strike to provide the strongest signal-to-noise ratio possible for the embedded FBG. Because of the unexpected and widely separated secondary response observed with sample BY-3, the scanned bandwidth was also adjusted before each strike in order fully capture the embedded FBG response. Thus, the scanning rate for this sample varied depending upon the bandwidth of the window scanned.

The general response progression for sample BY-4 shared many of the characteristics described in the preceding sections. The initial transient strike response (Figure 3.41) consisted of a compression response occurring over the first two frequency sweeps. The compression response quickly diminished and a tension response dominated by strike 06 (Figure 3.42). Also by strike 06, the single peak observed in strike 01 had split into several separate peaks. This trend of further splitting and broadening continued in an extreme fashion until strike 22, at which point the extremely broadened response suddenly returned to a strong main peak. Following this change, the response continued to exhibit only a tensile strain response through the remainder of the sample life, as shown in strike 24 (Figure 3.43).

Similar to the responses in samples BY-1 and BY-2, the intensity of the transient response increased dramatically during the first and last scans of the strike event for several impacts (Figure 3.44). The intensity increase relative to the quasi-static response before and after the strike is large enough that a broad area of the peak is saturated. Noticeably absent

from the BY-4 response was the smooth matrix relaxation observed in the previous samples. Even in the next to last and last strikes (Figure 3.45 and Figure 3.46), little to no Bragg wavelength shift is observed during or after the transient response.

The most interesting feature of sample BY-4 was the widely separated split peaks. Beginning with strike 05 through strike 22, the embedded grating response split into several groups of separate peaks that began to diverge (Figure 3.47 and Figure 3.48). In strike 05, the total bandwidth of the peaks covers approximately one nanometer. By strike 14, the group covered over 6nm, and at the widest separation, the spectral band is over 16nm wide. Due to the wide separation, the embedded grating response overlapped and even passed the reference grating response. Obviously, this response cannot be generated by transverse compressive loading of the grating even in its most extreme. One notable difference between the BY-4 response and the super-structuring responses observed in previous samples is the lack of a response at the original position of the embedded grating. By strike 14, only minor sub-structuring is observed around the embedded FBG Bragg wavelength, with the strong peaks located several nanometers on either side.

When comparing the FBG behavior to the impact characterization data (Figure 3.49), nothing indicative of the super-structuring response is noted. The generalized “critical damage” point where dissipated energy increases occurs approximately at strike 40. There is no clearly defined change in the transient FBG response around this point in the high speed full spectrum data for this sample.

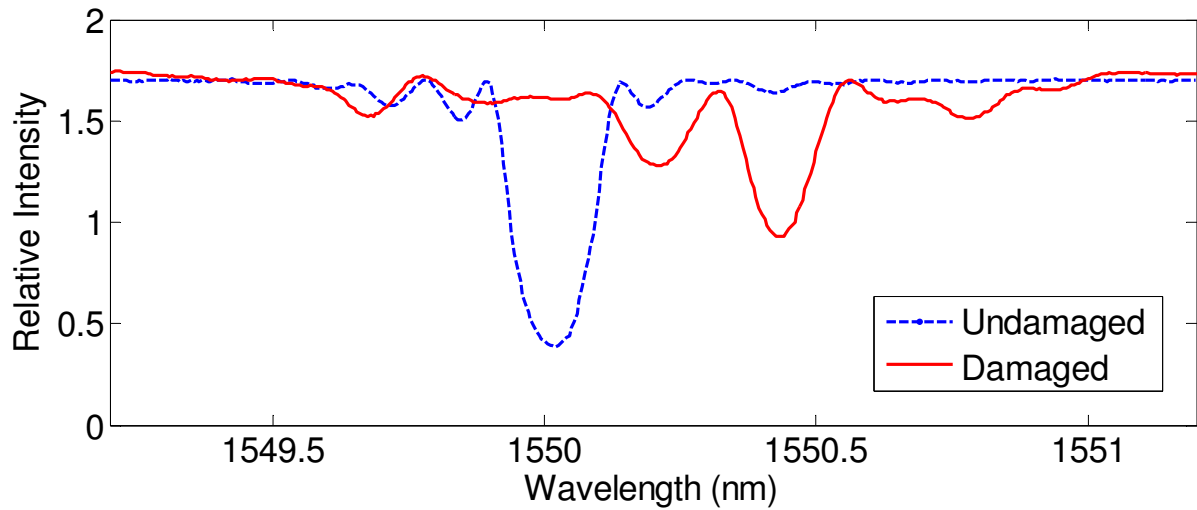


Figure 3.1 Low speed, full spectrum data for embedded sensor before and after impact damage (S-3, strike 00 and strike 08).

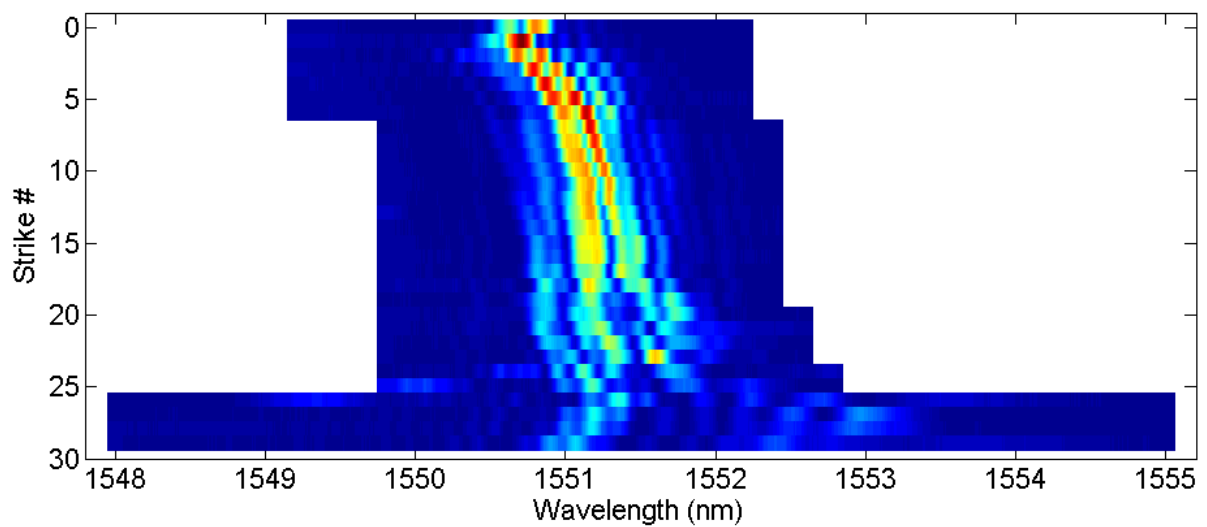


Figure 3.2 Low speed, full spectrum data for sample S-4 (sensor failed on strike 30 of 79). For this and all later spectral sweep plots, red indicates maximum intensity; dark blue indicates minimum intensity.

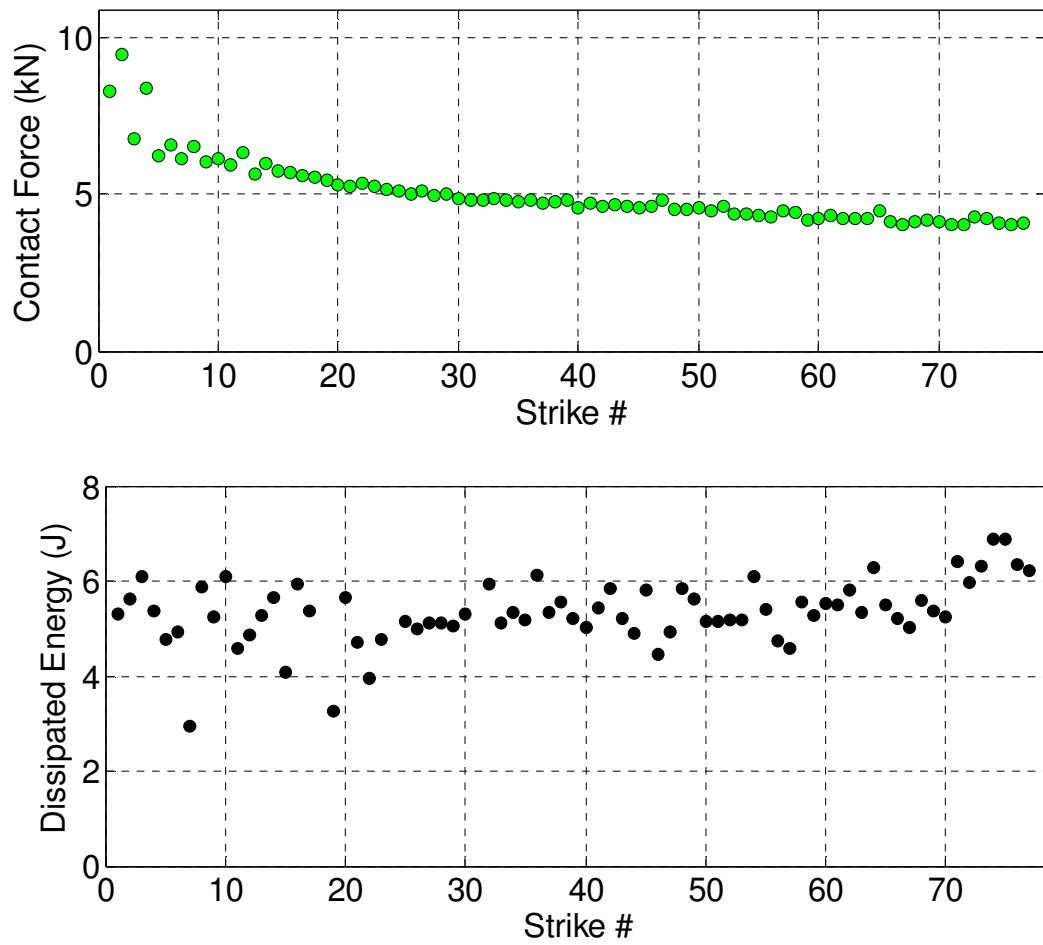
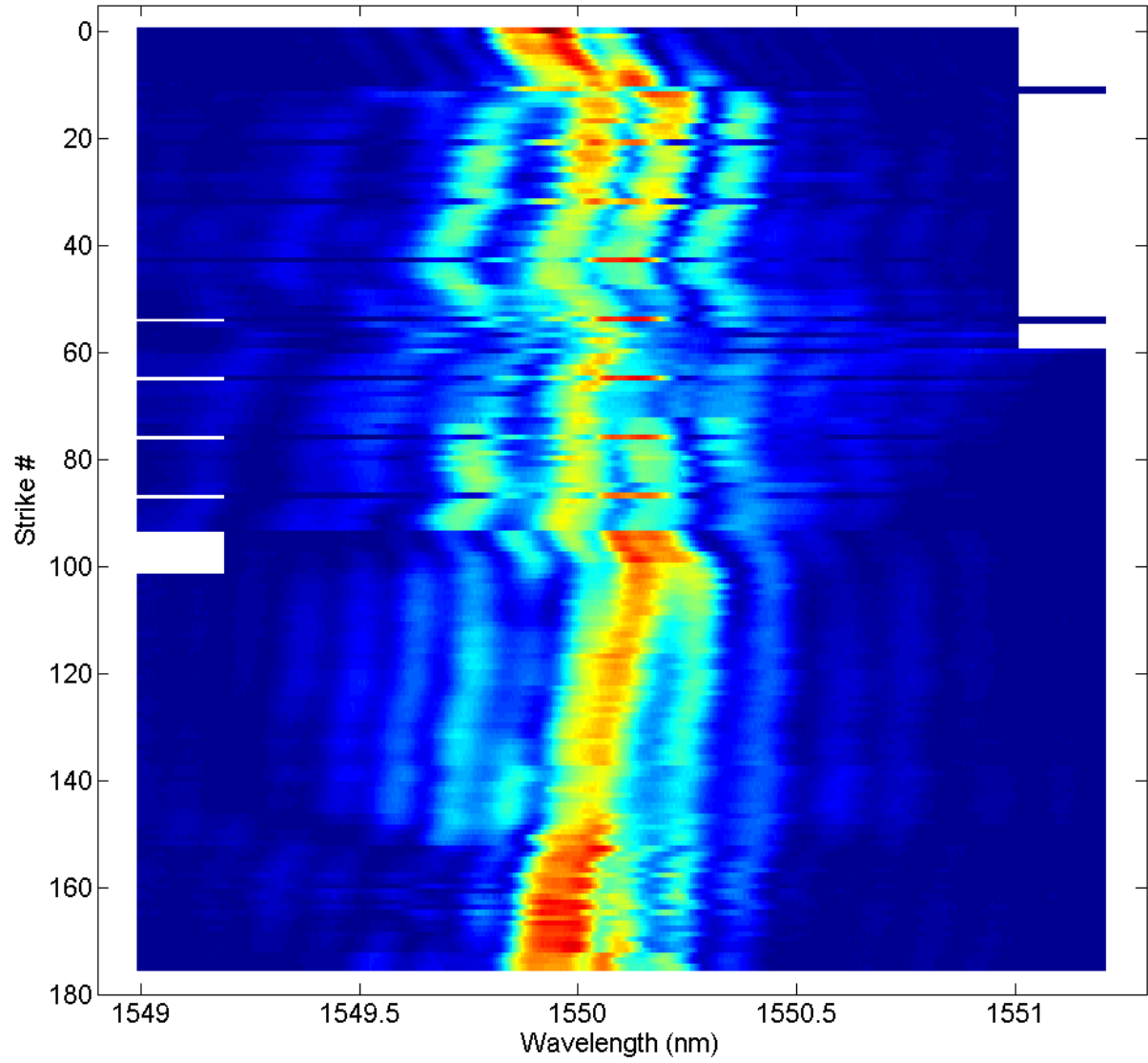


Figure 3.3 Contact force between impactor and the sample (top) and energy dissipated over the life of the sample (bottom) for S-4.



**Figure 3.4** Low speed, full spectrum data for sample S-6.

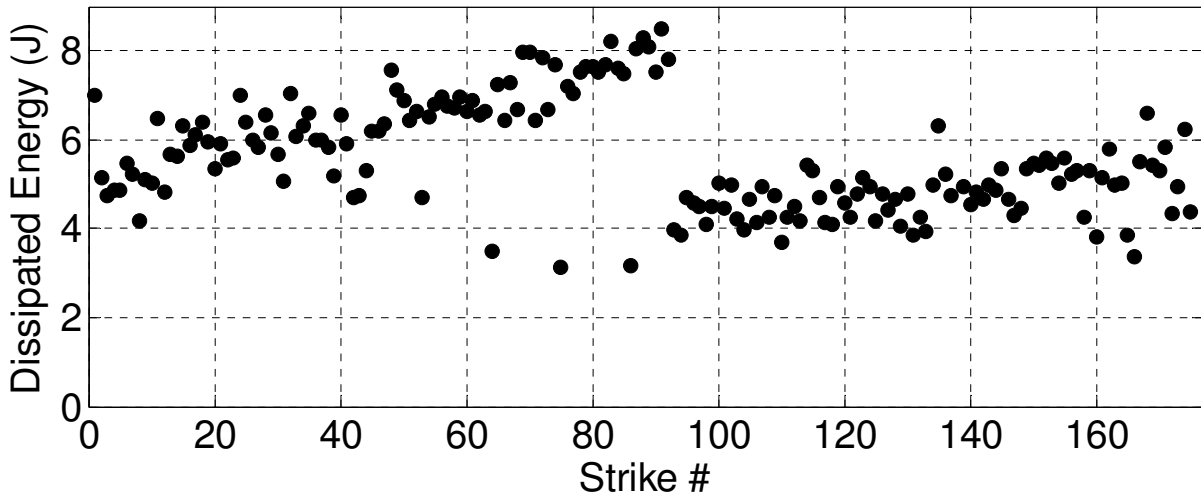
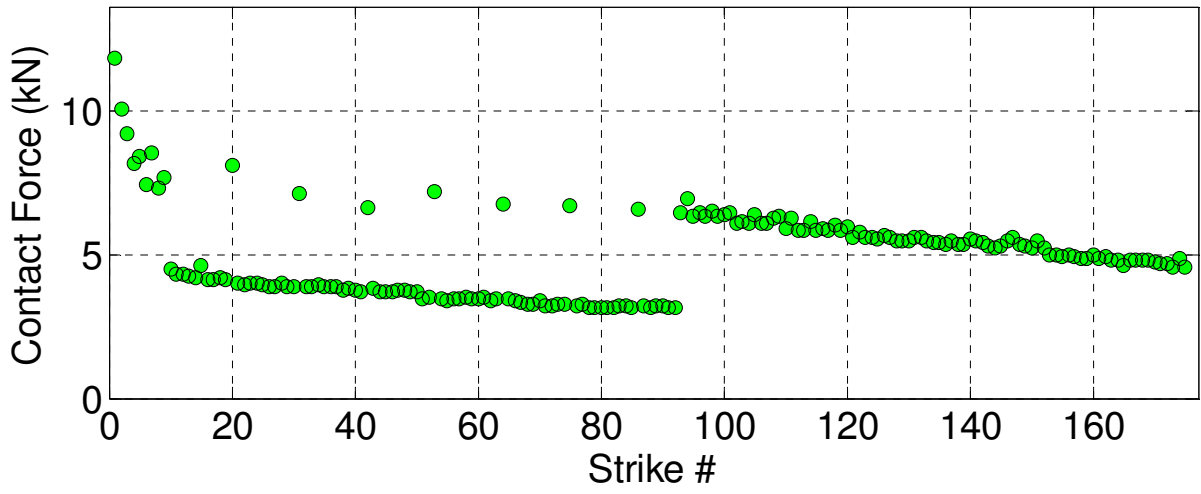
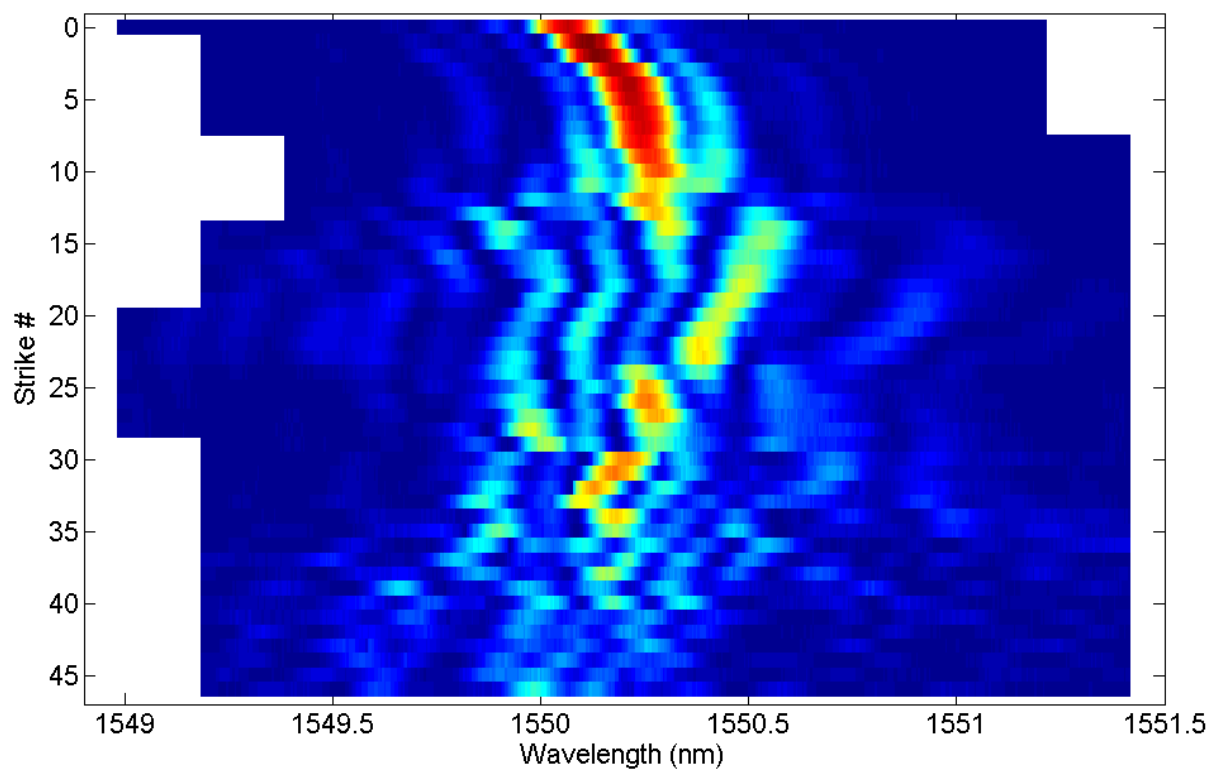


Figure 3.5 Contact force between impactor and the sample (top) and energy dissipated over the life of the sample (bottom) for S-6.



**Figure 3.6** Low speed, full spectrum data for sample S-7.

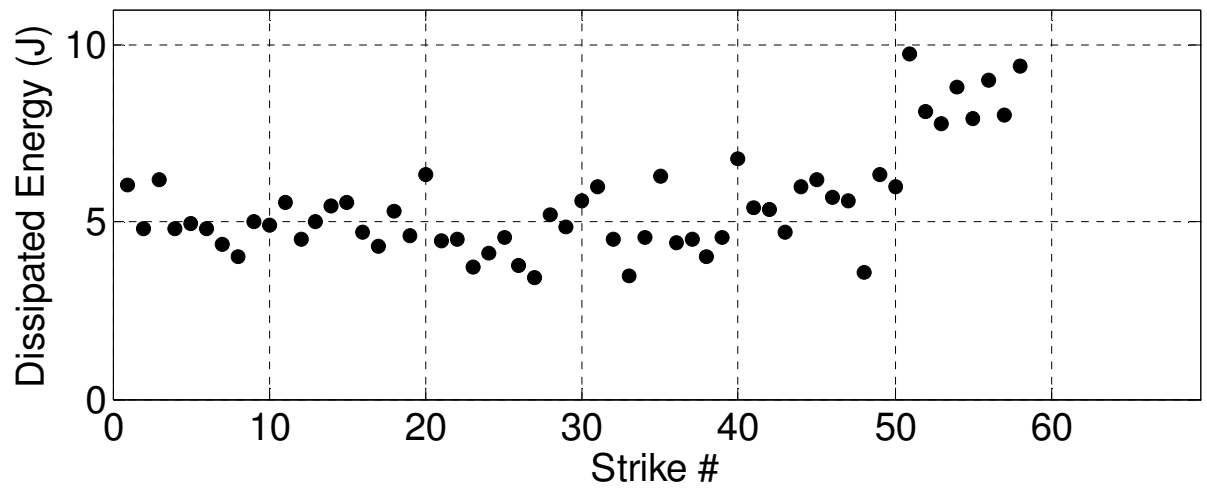
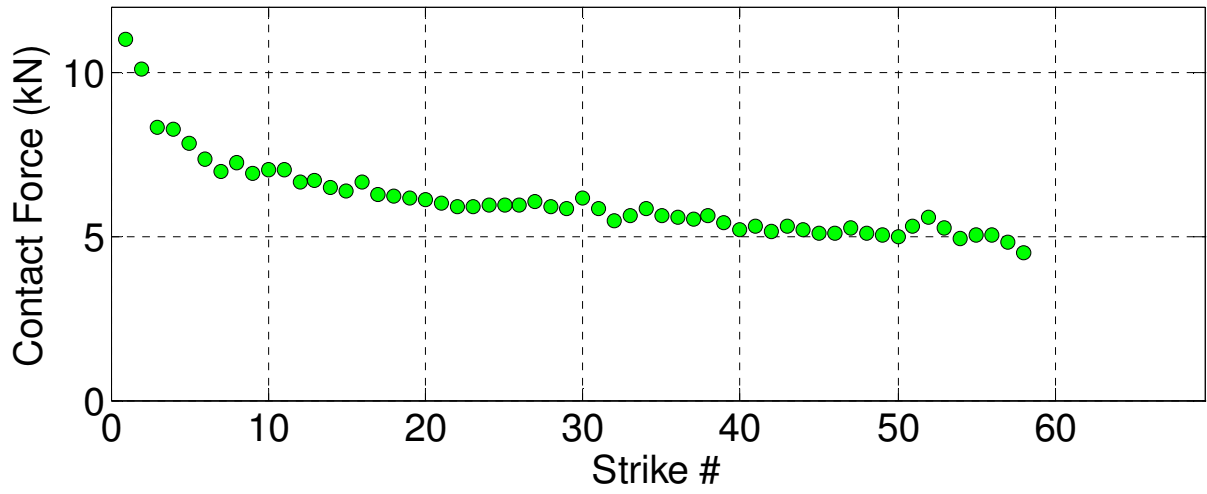


Figure 3.7 Contact force between impactor and the sample (top) and energy dissipated over the life of the sample (bottom) for S-7.

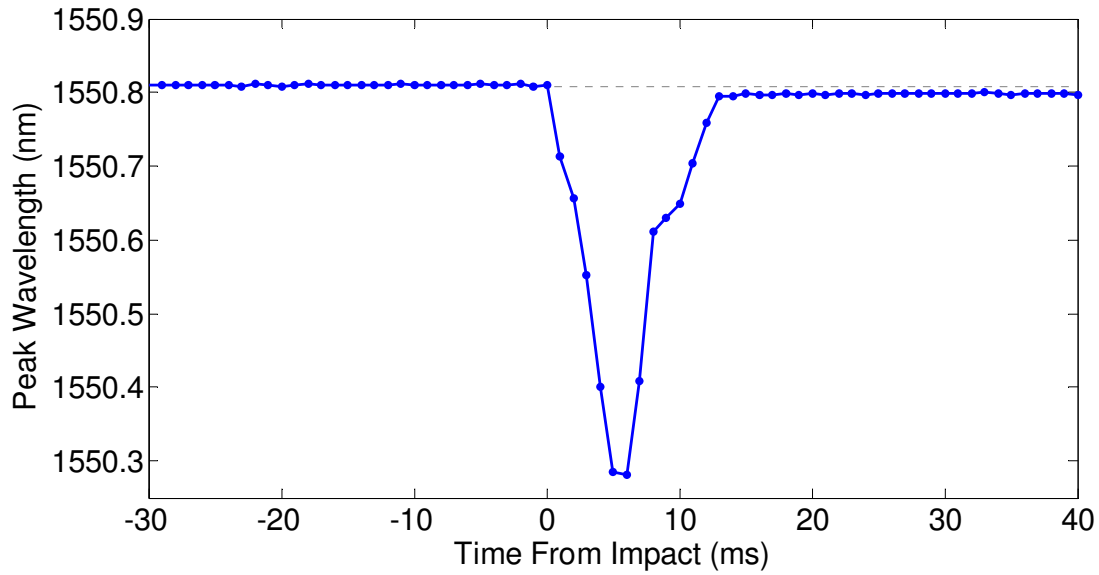


Figure 3.8 High speed, peak wavelength data showing typical FBG response (S-1, strike #36).

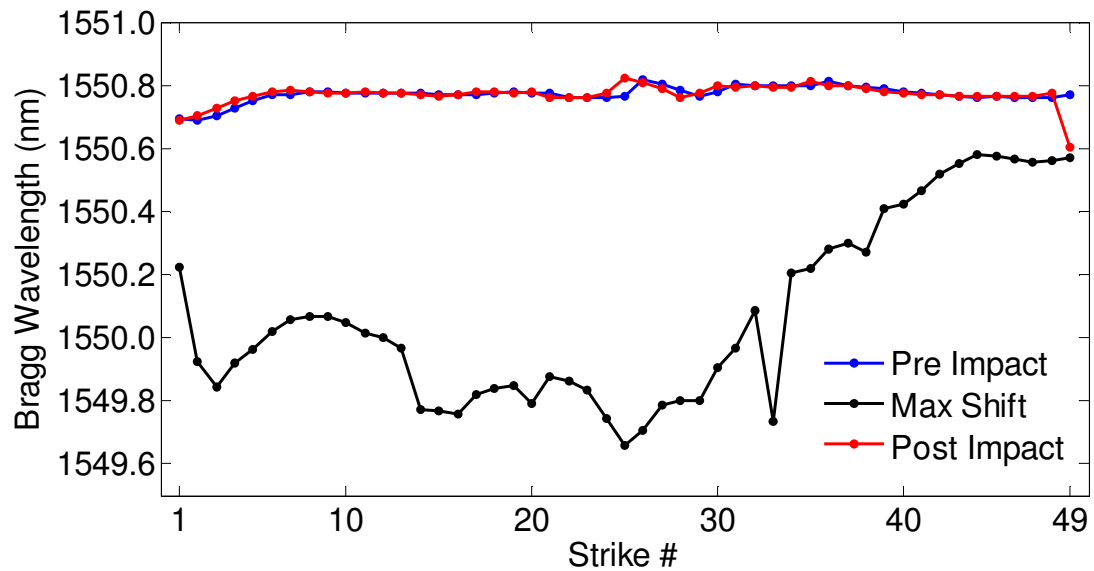


Figure 3.9 High speed, peak wavelength data showing the Bragg wavelength 50ms before (blue) and 50ms after (red) the impact event, along with the Bragg wavelength at the point of maximum shift during the event itself (black) for sample S-1.

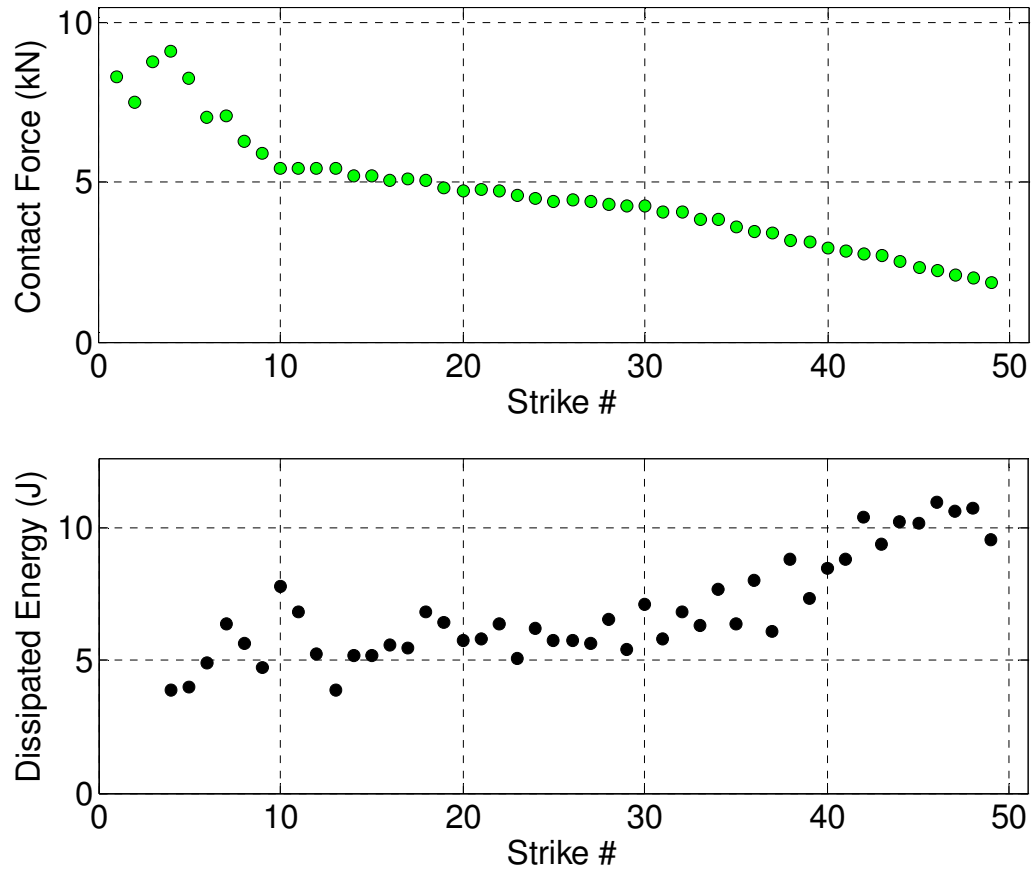
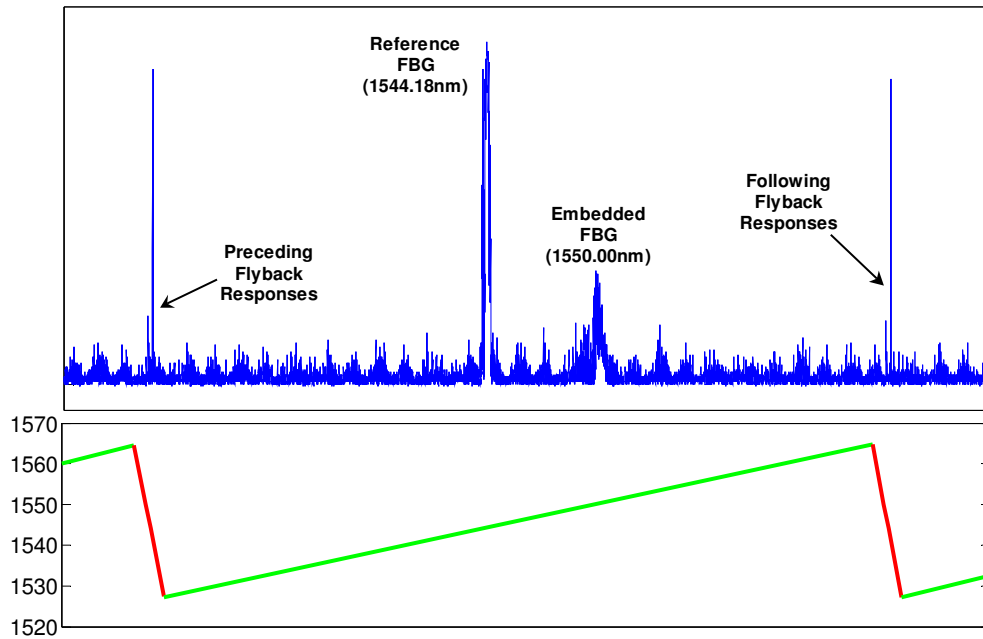


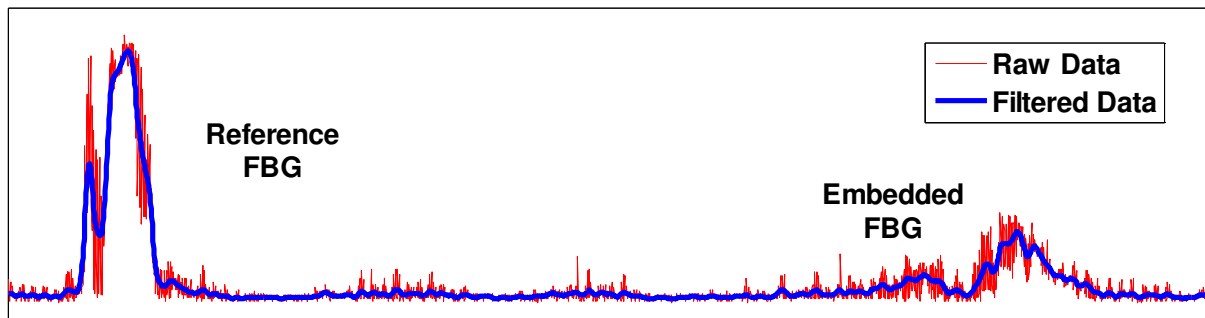
Figure 3.10 Contact force between impactor and the sample (top) and energy dissipated over the life of the sample (bottom) for S-1. Dissipated energy data was not collected for strikes 1-3.

Table 3.1. Samples with FBG sensors interrogated using BYU's FSIM instrumentation.

Sample Number	BY-1	BY-2	BY-3	BY-4
Energy Per Strike (J)	11.0	12.4	13.9	12.4
Strikes to Failure	31	82	12	49
Distance to Grating (in)	0.50	0.63	0.50	0.50
Full Spectral Scan Rate (Hz)	200	534	926	Variable
Interrogation Description	Data recorded using NCSU's analog-digital converter	Fixed window, Fixed EDFA power	Fixed window, Variable EDFA power	Variable window, Variable EDFA power



**Figure 3.11** High speed, full spectrum raw data (top) showing a single frequency sweep in the continuous data stream capturing the reference and embedded FBGs and the flyback responses between this sweep and the sweeps preceding and following it. The corresponding saw-tooth scanning pattern of the MEMS filter (bottom) falls between approximately 1530nm and 1560nm. The main sweeps are colored green while the flybacks are colored red (BY-1, strike #05).



**Figure 3.12** High speed, full spectrum raw and filtered data showing the reference and embedded grating responses in a single frequency sweep (BY-1, strike #05).

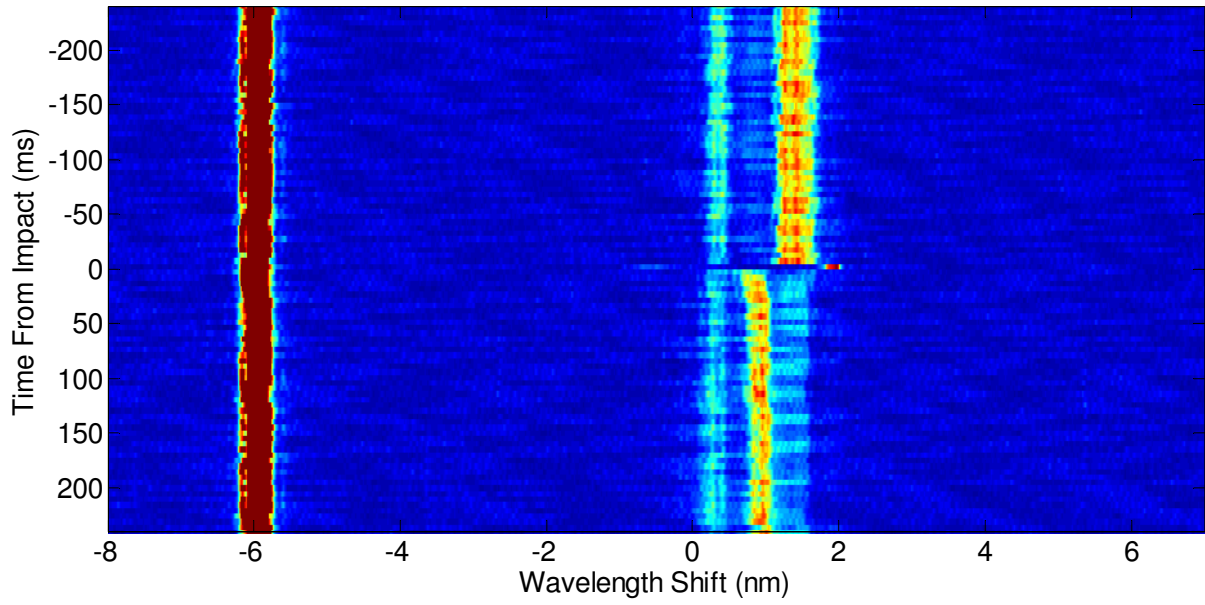


**Figure 3.13** Full image of high speed, full spectrum data for a single strike showing the reference grating on the left and the embedded grating response on the right (BY-1, strike #19).

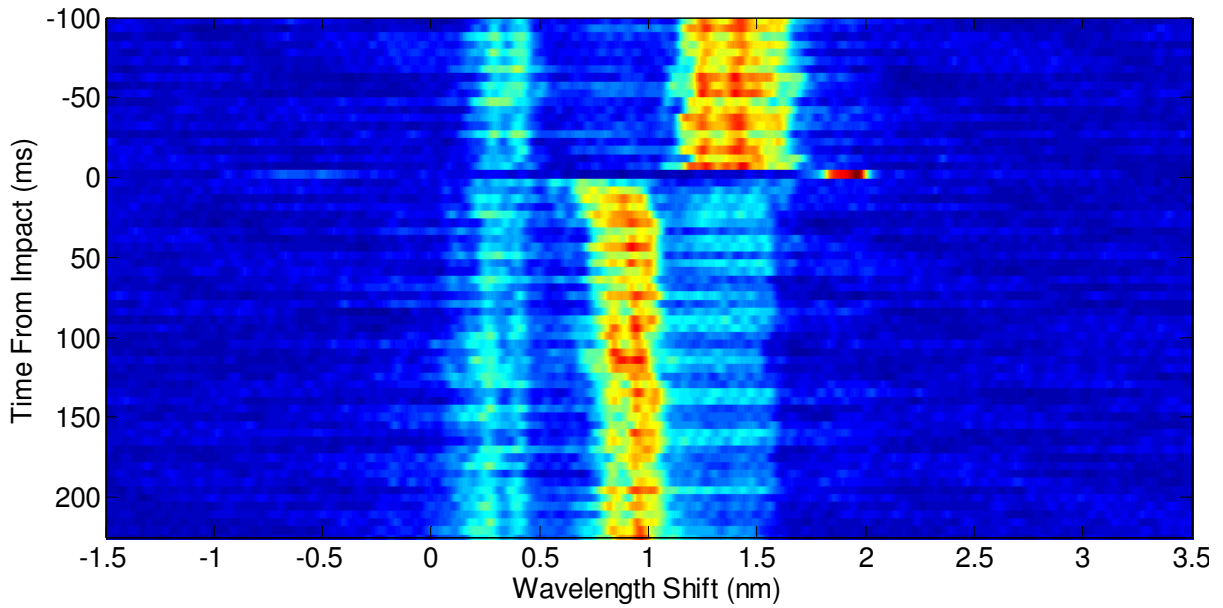


**Figure 3.14** Close-up image of high speed, full spectrum data for at the time of impact for a single strike showing only the embedded grating response (BY-1, strike #19).

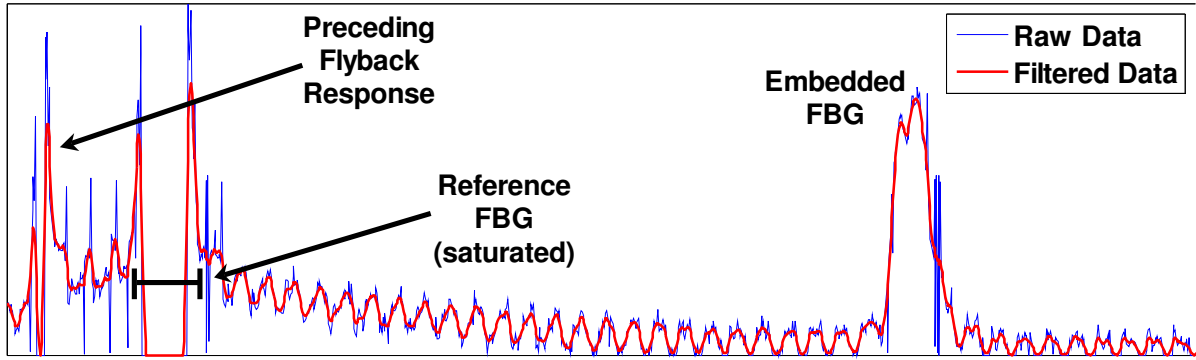


Figure 3.15 High speed, full spectrum raw and filtered data showing the reference and embedded grating responses in a single frequency sweep (BY-2, strike #01).

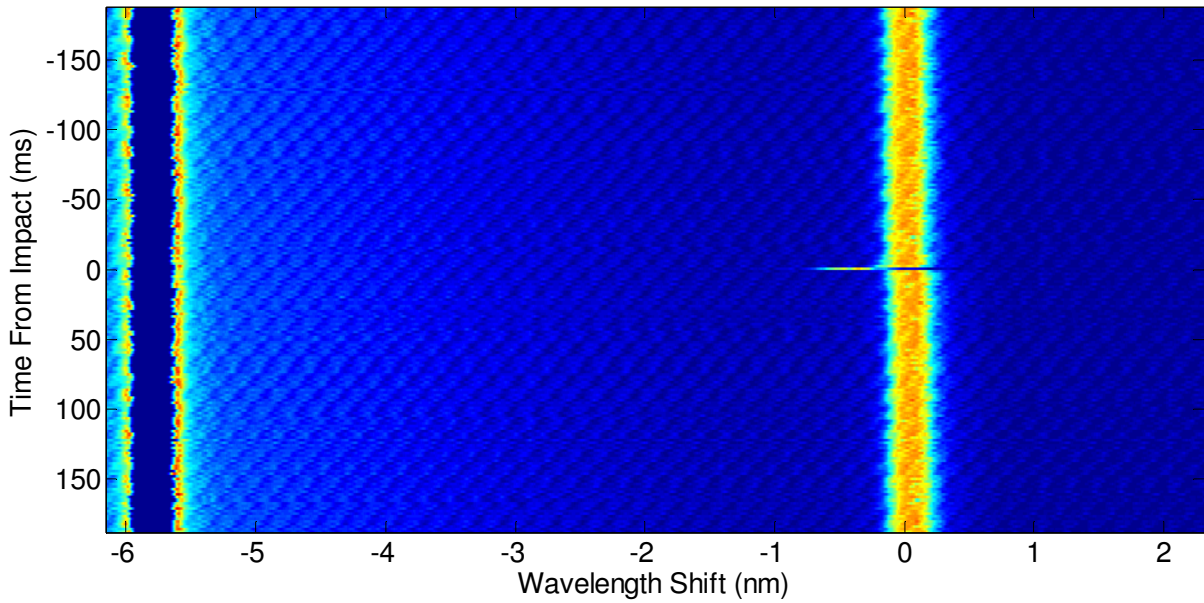
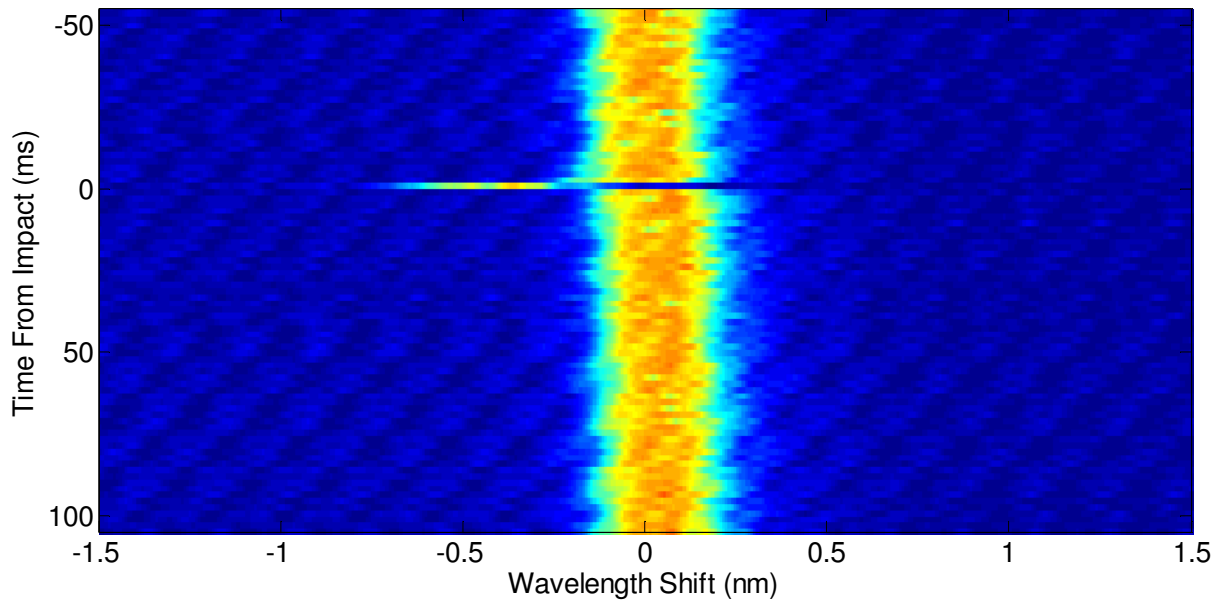


Figure 3.16 Full image of high speed, full spectrum data for a single strike showing reference grating on the left and the embedded grating response on the right (BY-2, strike #01).



**Figure 3.17** Close-up image of high speed, full spectrum data for at the time of impact for a single strike showing only the embedded grating response (BY-2, strike #01).

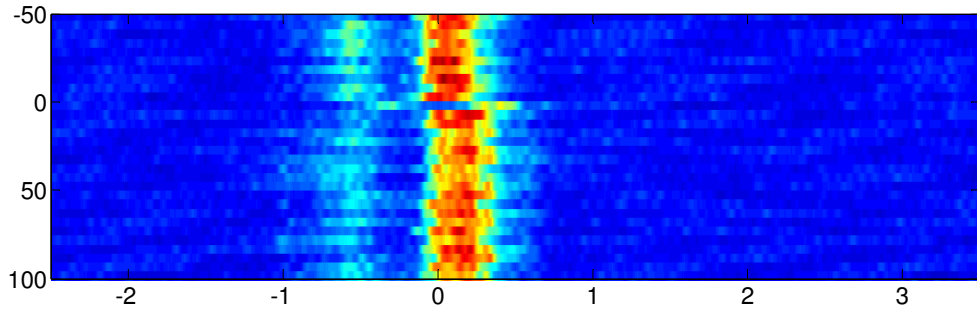


Figure 3.18 Image of strike #07 response for sample BY-1.<sup>2</sup>

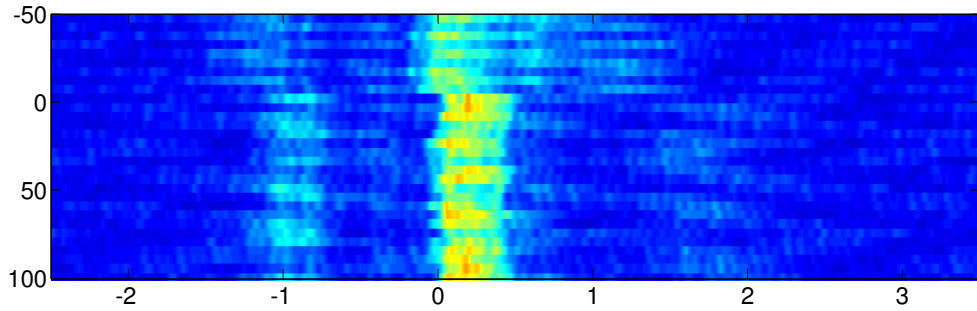


Figure 3.19 Image of strike #09 response for sample BY-1.

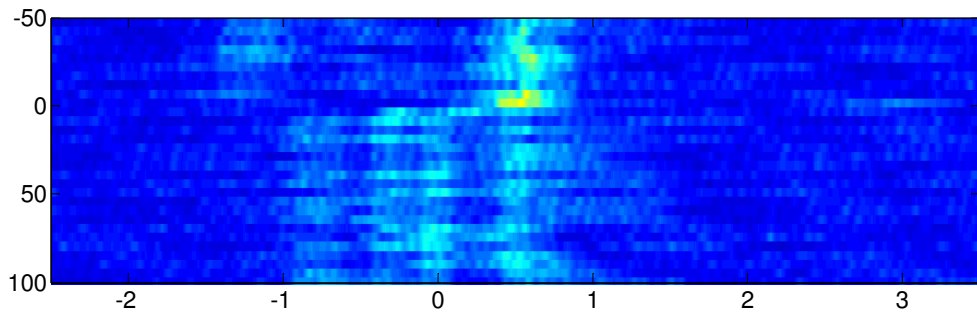


Figure 3.20 Image of strike #12 response for sample BY-1.

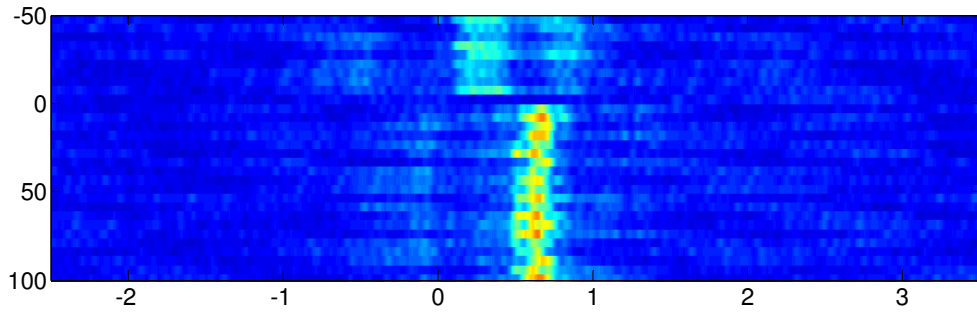
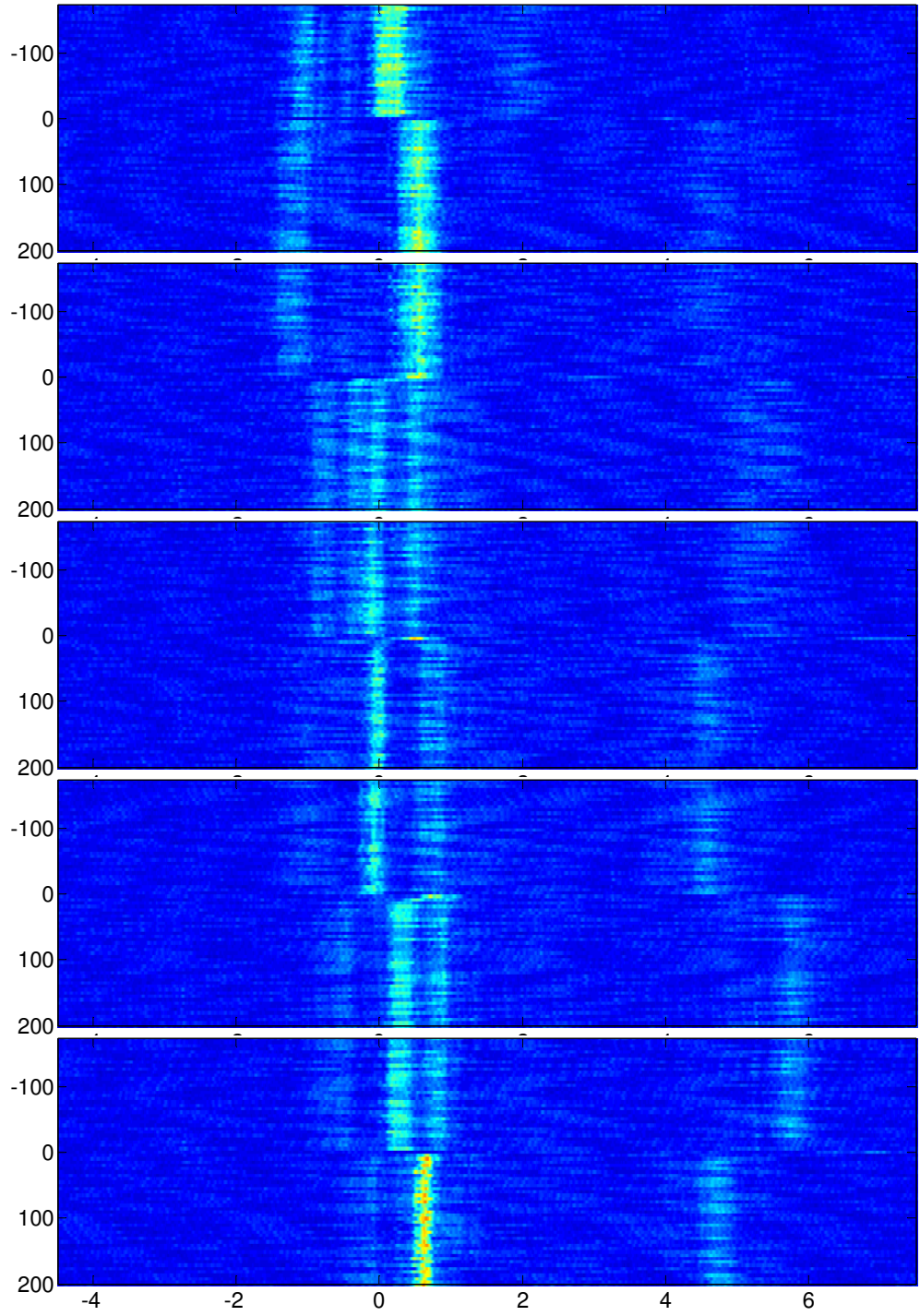


Figure 3.21 Image of strike #15 response for sample BY-1.

<sup>2</sup> This and all subsequent high speed, full spectrum data plots presented in this format consist of relative wavelength shift (nm) on the horizontal axis and time from impact (ms) on vertical axis.



**Figure 3.22** Images of responses for strikes 11 through 15 (from top to bottom) for sample BY-1 showing secondary response at wavelengths several nanometers longer than the primary response. Each image shows 150ms before and 200ms after the initial FBG response during the strike event. The horizontal axes show wavelength shift (nm) from an initial reference point prior to damage.

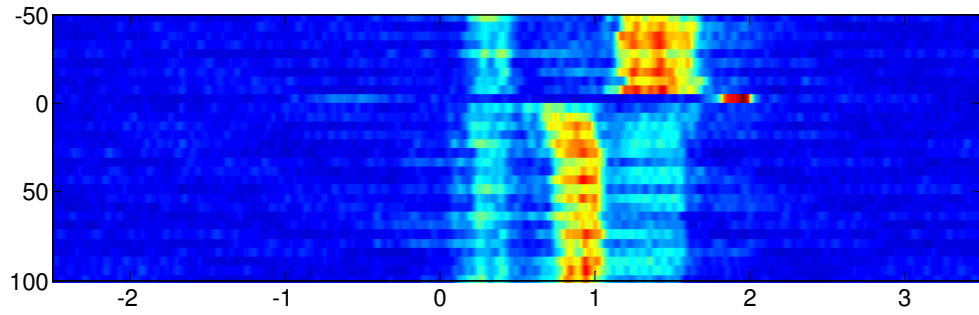


Figure 3.23 Image of strike #19 response for sample BY-1.

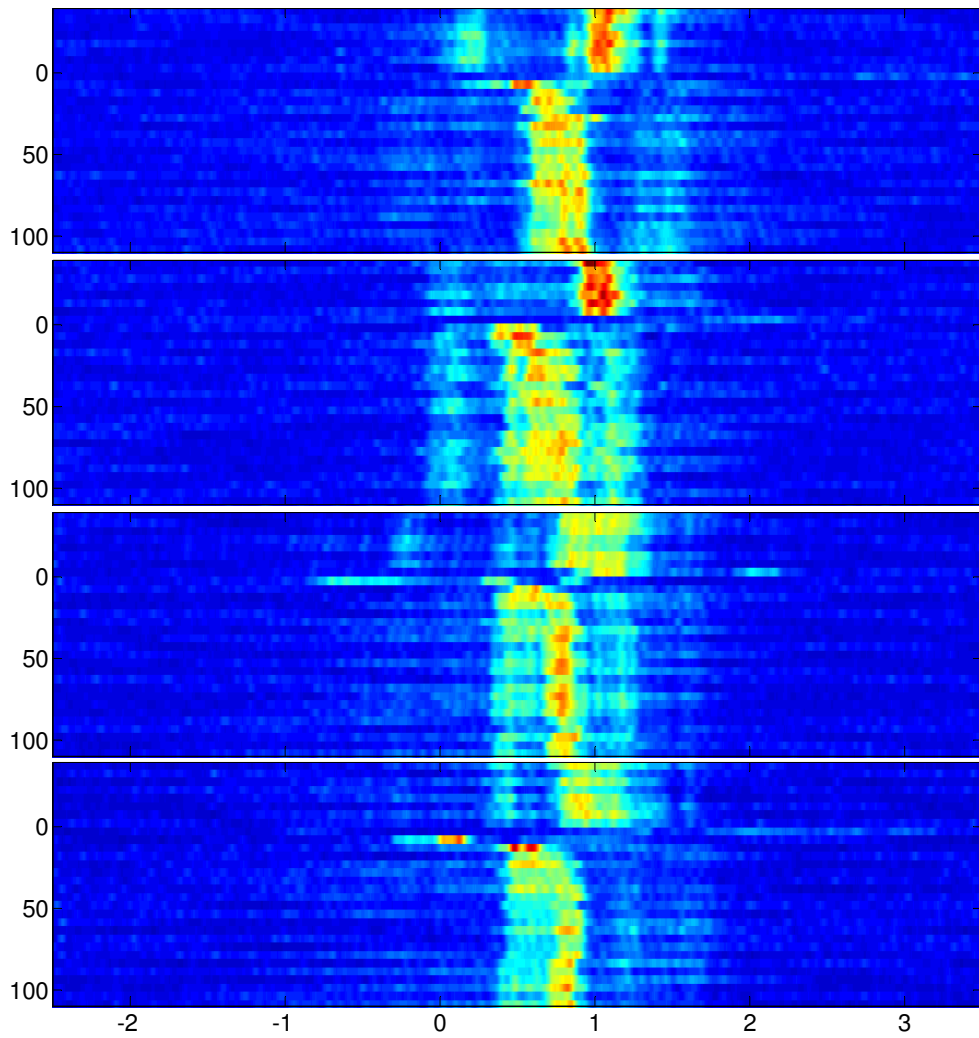


Figure 3.24 Images of responses during strikes 20, 22, 28, and 29 for sample BY-1 (from top to bottom) showing relaxation. Each image shows 40ms before and 110ms after the initial FBG response during the strike event. The horizontal axes show wavelength shift (nm) from an initial reference point prior to damage.

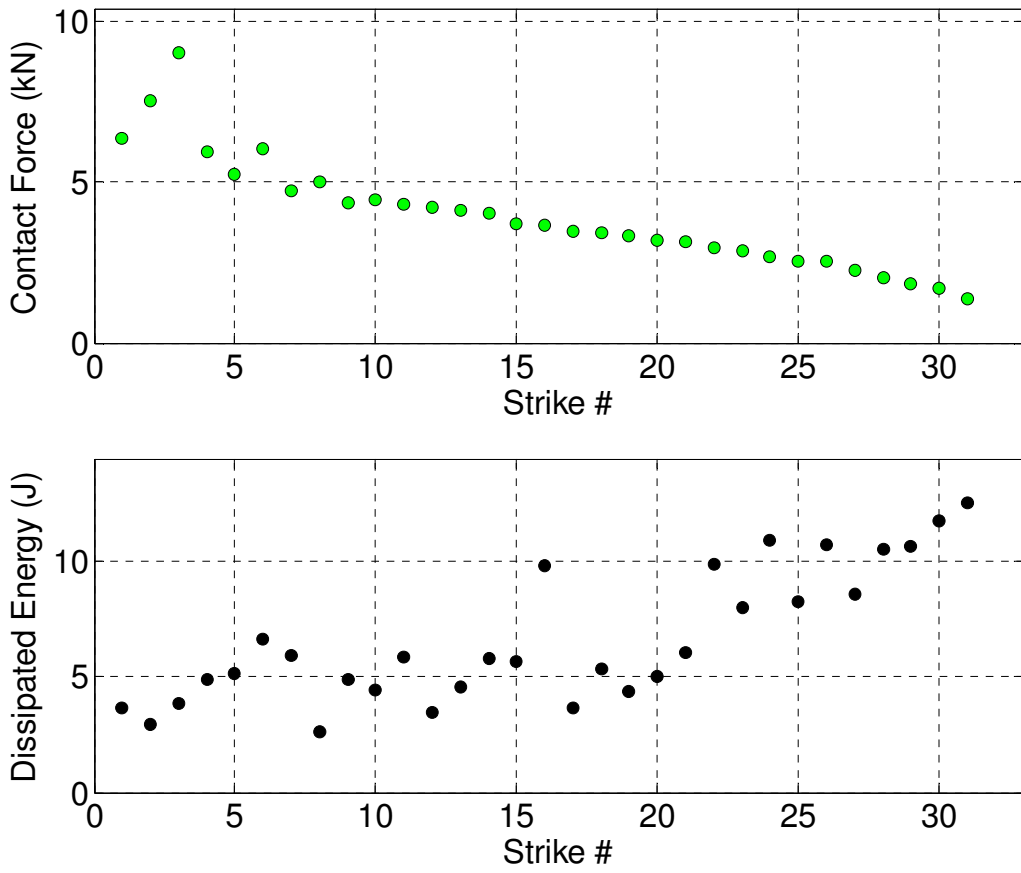


Figure 3.25 Contact force between impactor and the sample (top) and energy dissipated over the life of the sample (bottom) for BY-1.

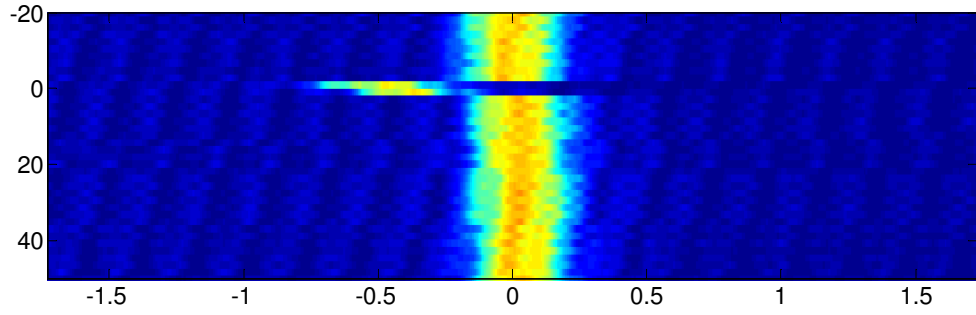


Figure 3.26. Image of strike #03 response for sample BY-2.

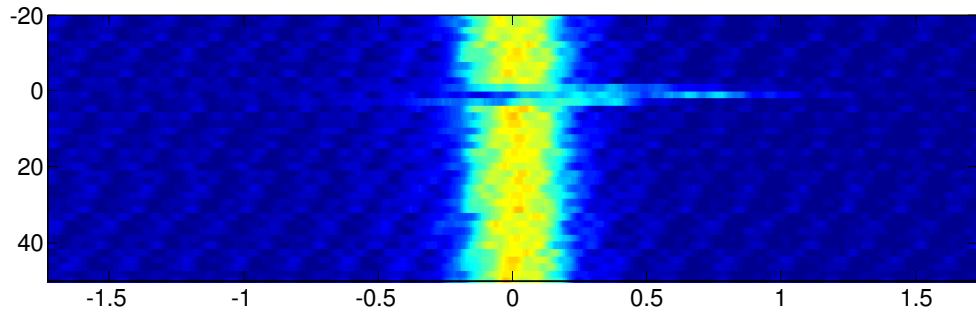


Figure 3.27. Image of strike #20 response for sample BY-2.

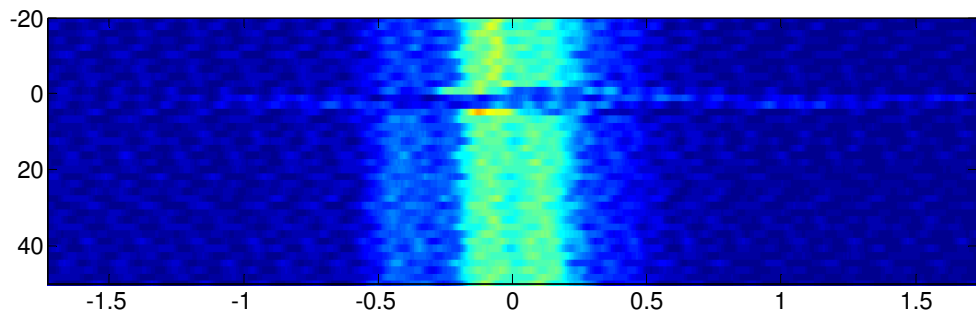


Figure 3.28. Image of strike #29 response for sample BY-2.

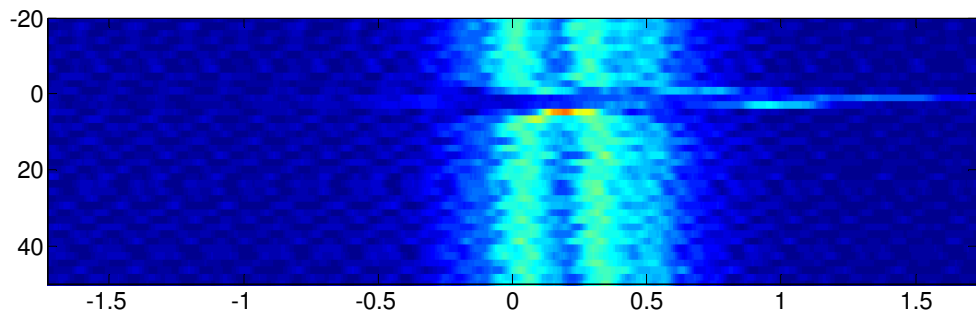
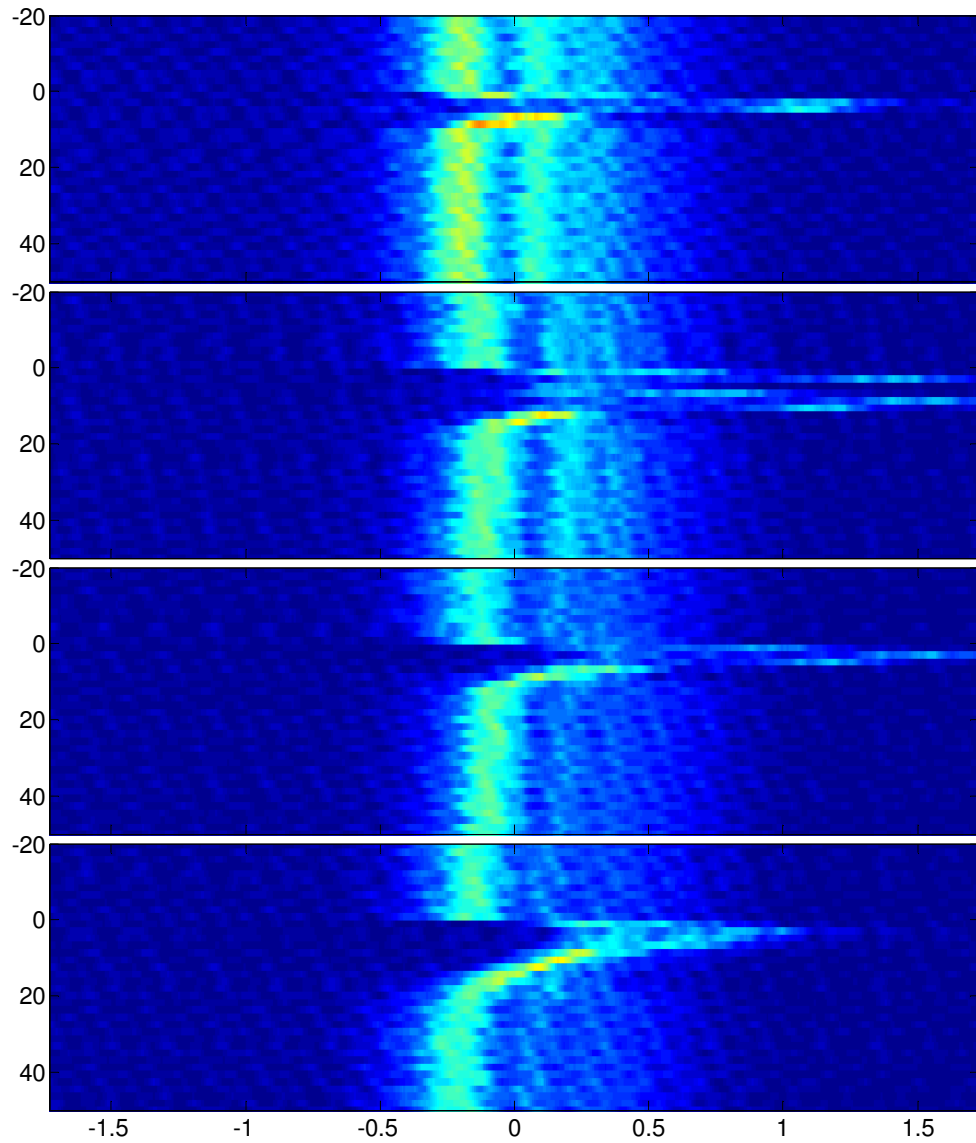
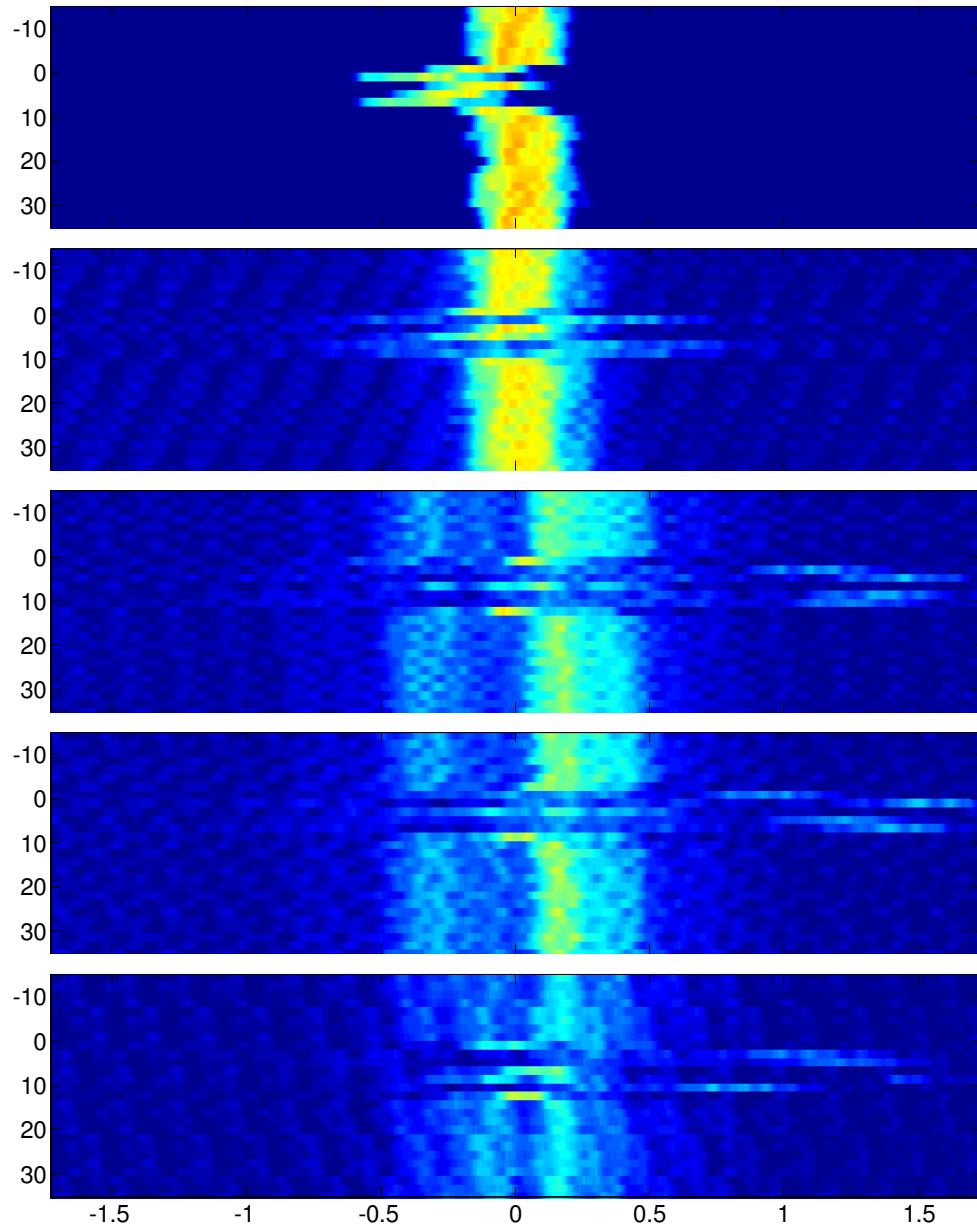


Figure 3.29. Image of strike #65 response for sample BY-2.



**Figure 3.30. Progression of FBG relaxation responses during strikes 67, 77, 79, and 81 (from top to bottom) for sample BY-2. Each image shows 20ms before and 50ms after the initial FBG response during the strike event. The horizontal axes show wavelength shift (nm) from an initial reference point before each strike.**



**Figure 3.31. Oscillatory FBG responses during strikes 6, 15, 39, 42, and 53 (from top to bottom) for sample BY-2. Each image shows 15ms before and 35ms after the initial FBG response during the strike event. The horizontal axes show wavelength shift (nm) from an initial reference point before each strike.**

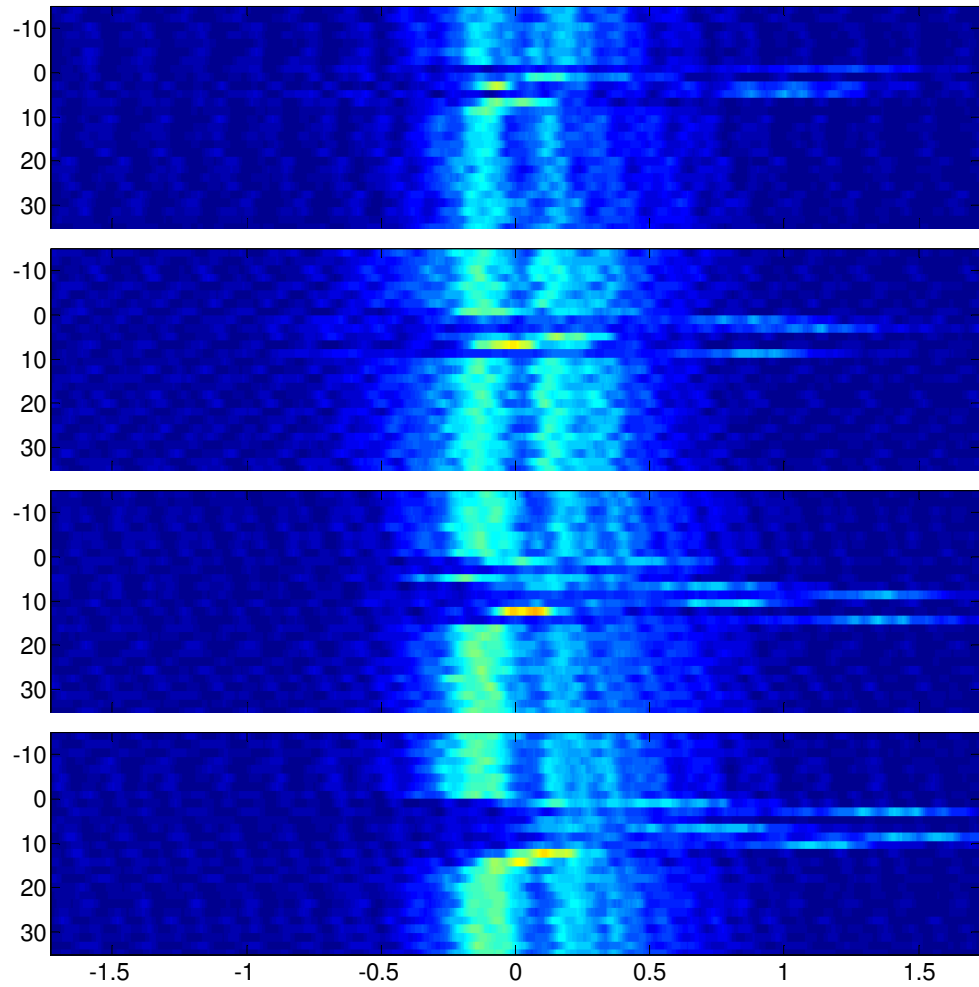


**Figure 3.32. Oscillatory FBG responses during strikes 61, 64, 68, and 77 (from top to bottom) for sample BY-2. Each image shows 15ms before and 35ms after the initial FBG response during the strike event. The horizontal axes show wavelength shift (nm) from an initial reference point before each strike.**

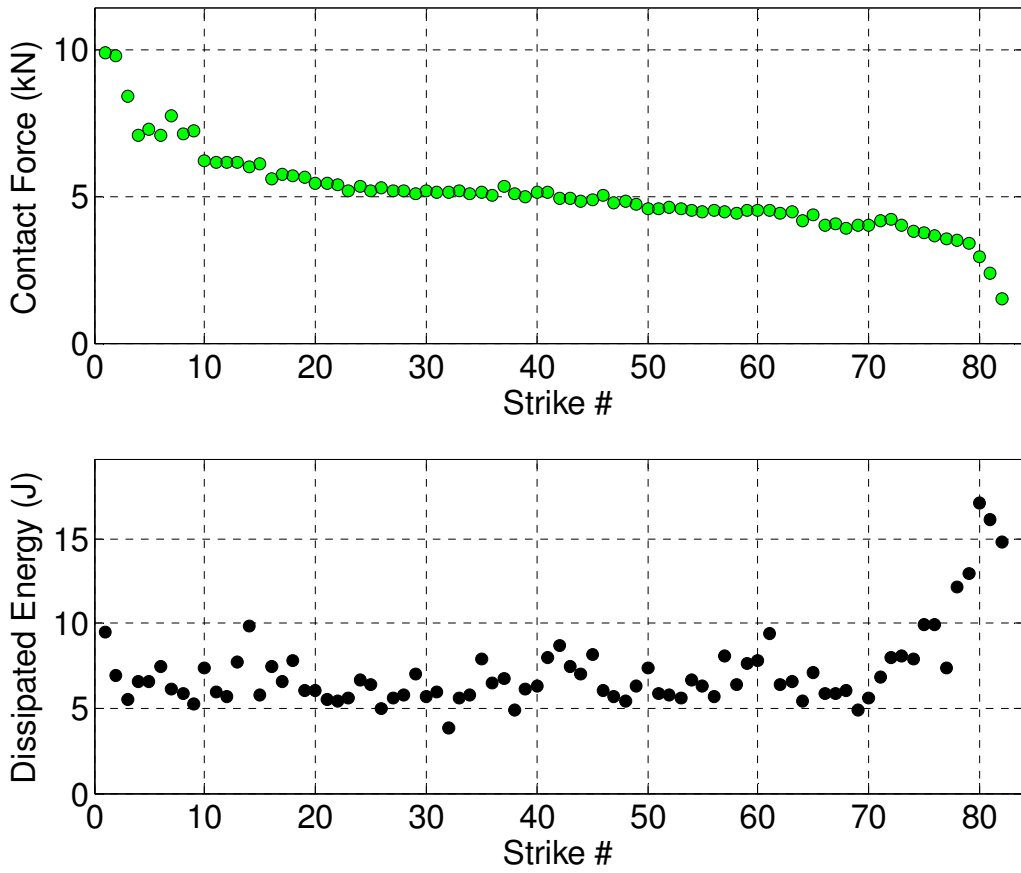


Figure 3.33 Contact force between impactor and the sample (top) and energy dissipated over the life of the sample (bottom) for BY-2.

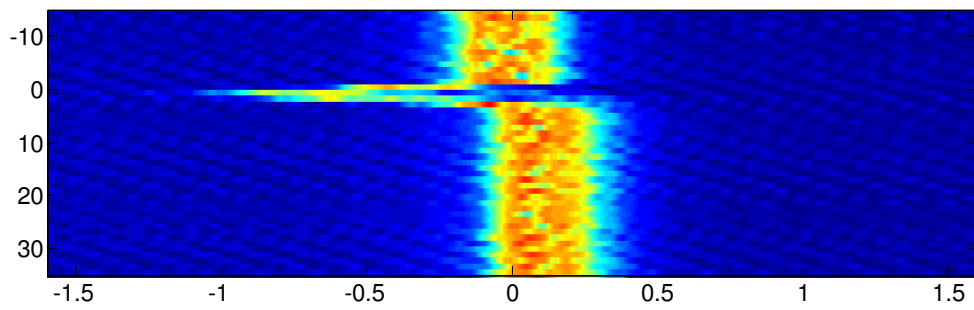
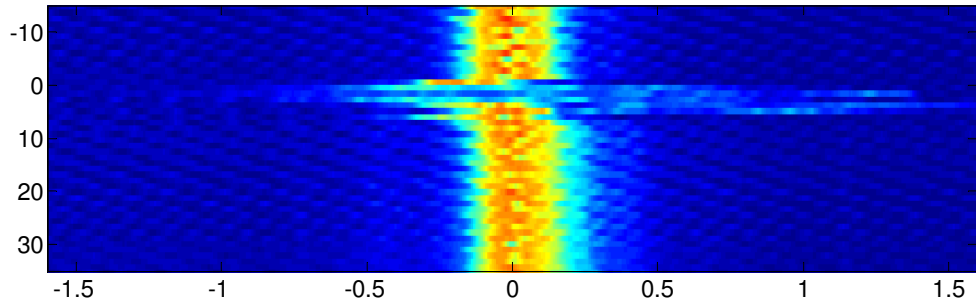
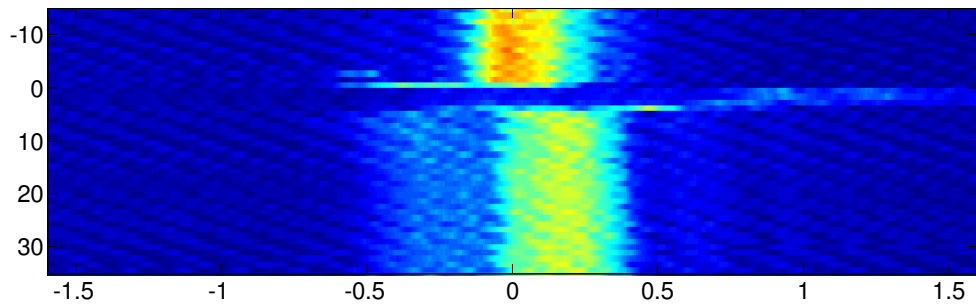


Figure 3.34 Image of strike #02 response for sample BY-3.



**Figure 3.35** Image of strike #04 response for sample BY-3.



**Figure 3.36** Image of strike #05 response for sample BY-3.

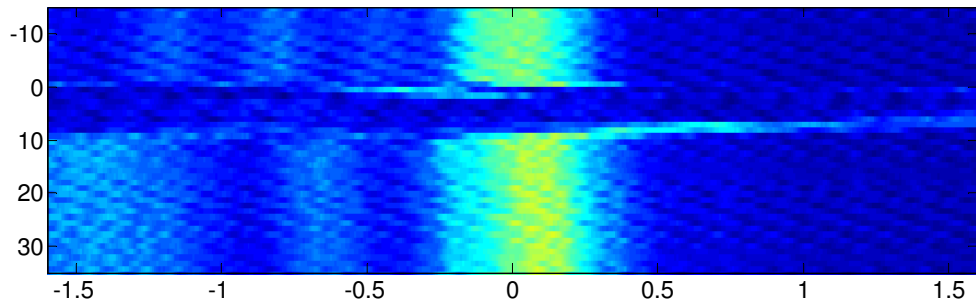


**Figure 3.37** Image of strike #11 response for sample BY-3.

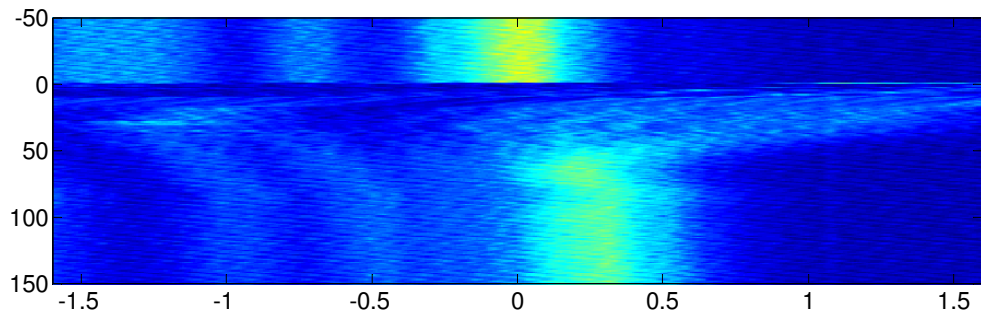


**Figure 3.38** Image of strike #12 response for sample BY-3.

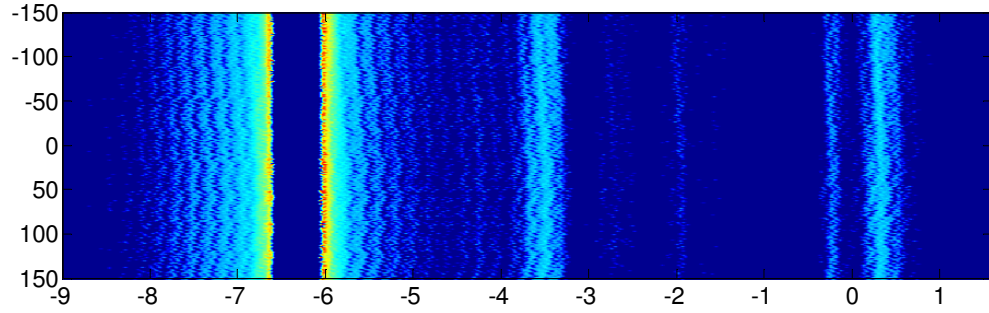


Figure 3.39 Wide bandwidth image of post-strike #09 response for sample BY-3.

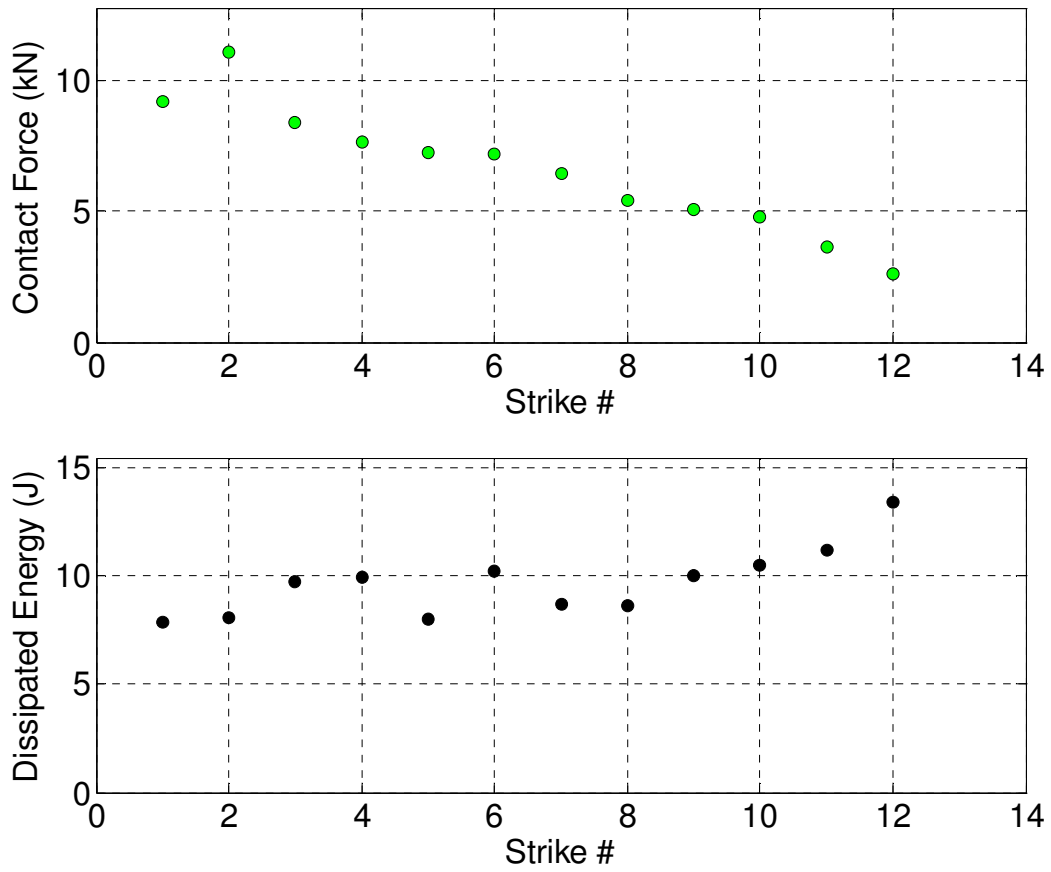
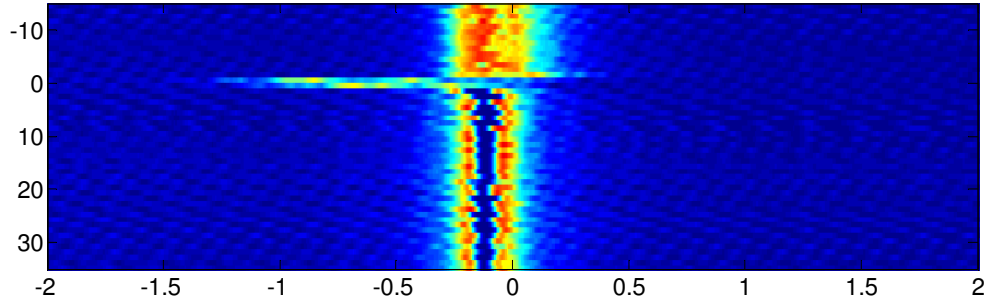
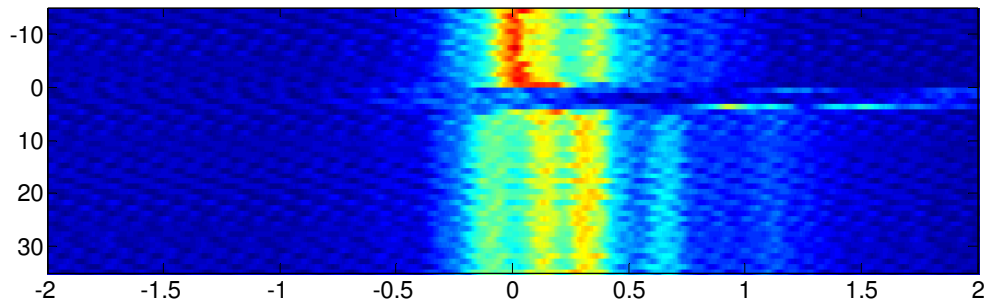


Figure 3.40 Contact force between impactor and the sample (top) and energy dissipated over the life of the sample (bottom) for BY-3.



**Figure 3.41** Image of strike #01 response for sample BY-4.



**Figure 3.42** Image of strike #06 response for sample BY-4.

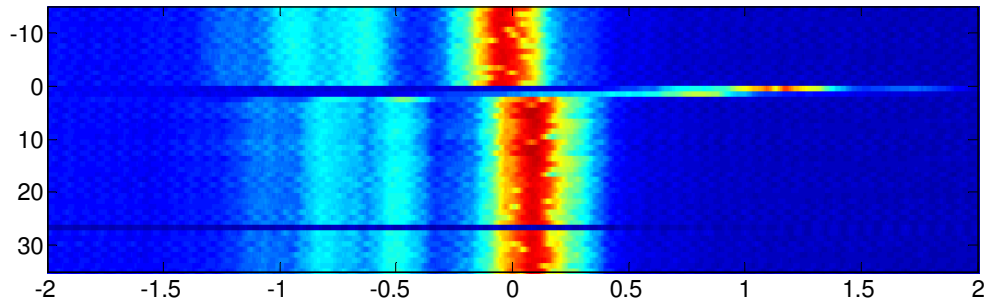


**Figure 3.43** Image of strike #24 response for sample BY-4.

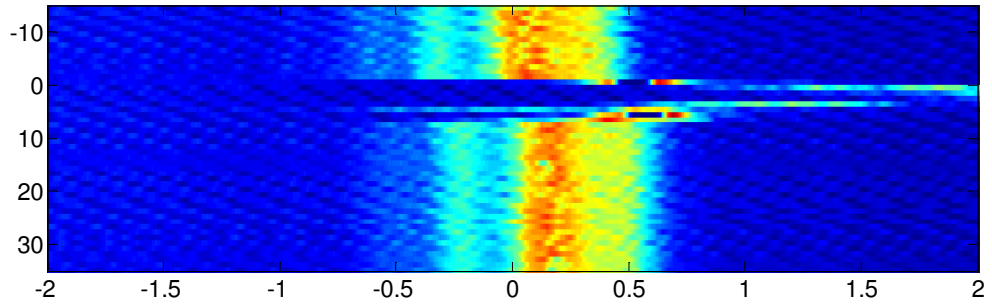


**Figure 3.44** Image of strike #26 response for sample BY-4.

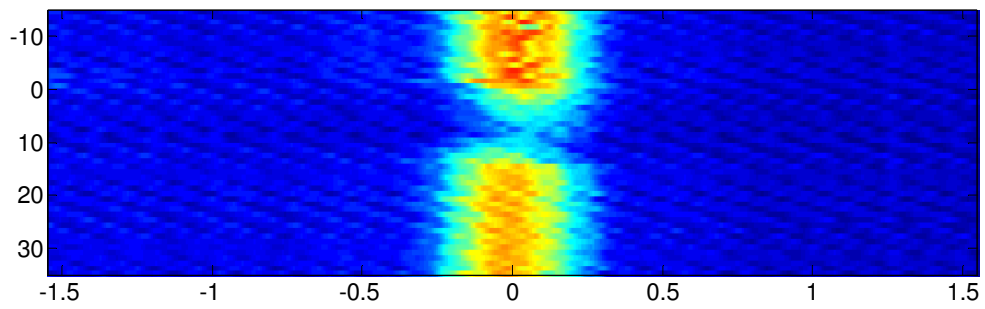


**Figure 3.45** Image of strike #48 response for sample BY-4.

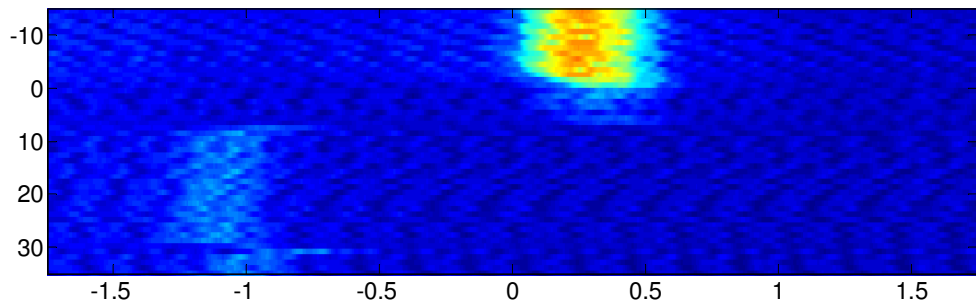


**Figure 3.46** Image of strike #49 response for sample BY-4.

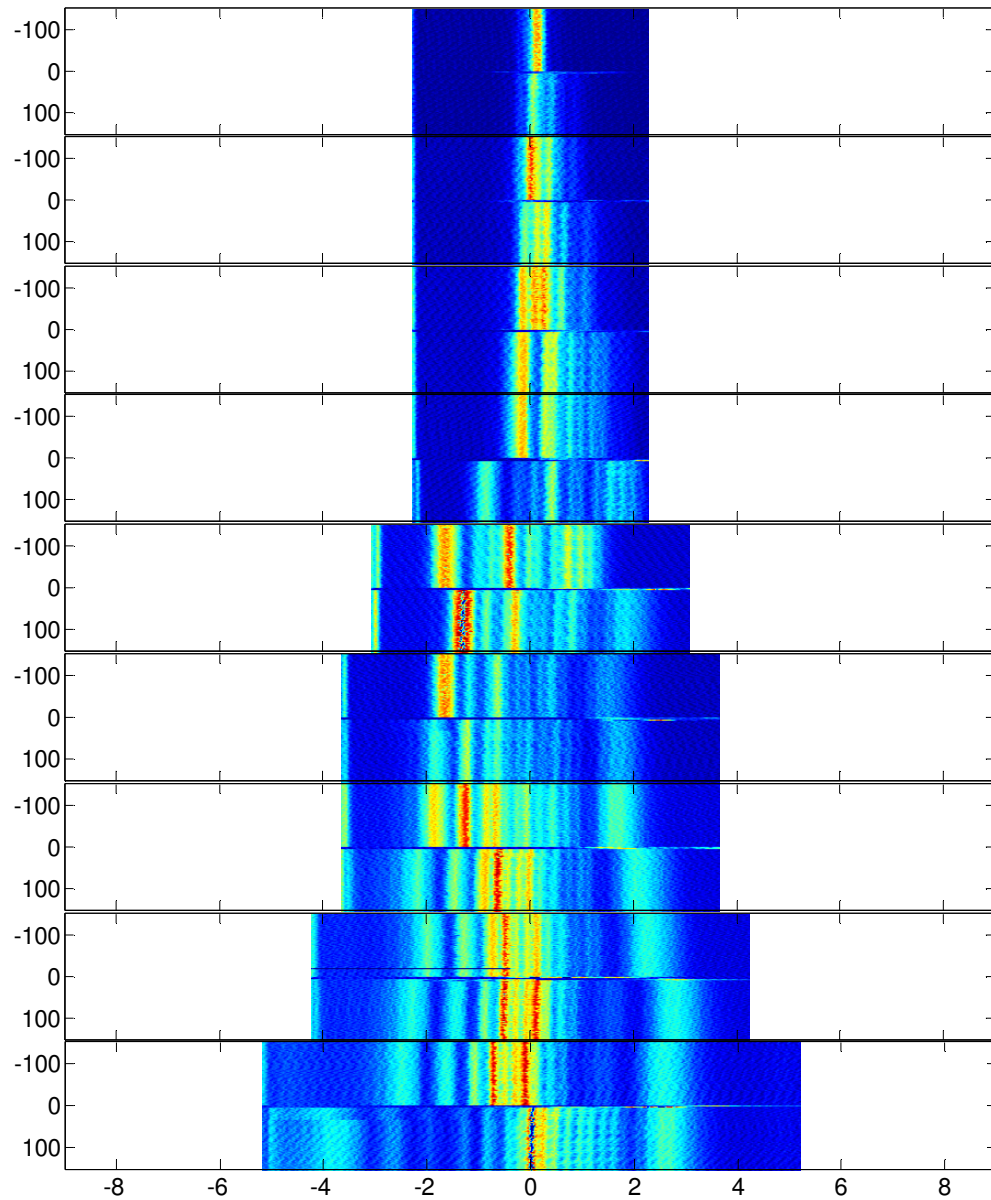


**Figure 3.47** Image of responses for strikes 05 through 13 (from top to bottom) for sample BY-4 showing secondary response at wavelengths several nanometers longer than the primary response. Each image shows 125ms before and 125ms after the initial FBG response during the strike event. The horizontal axes show wavelength shift (nm) from an initial reference point prior to damage..

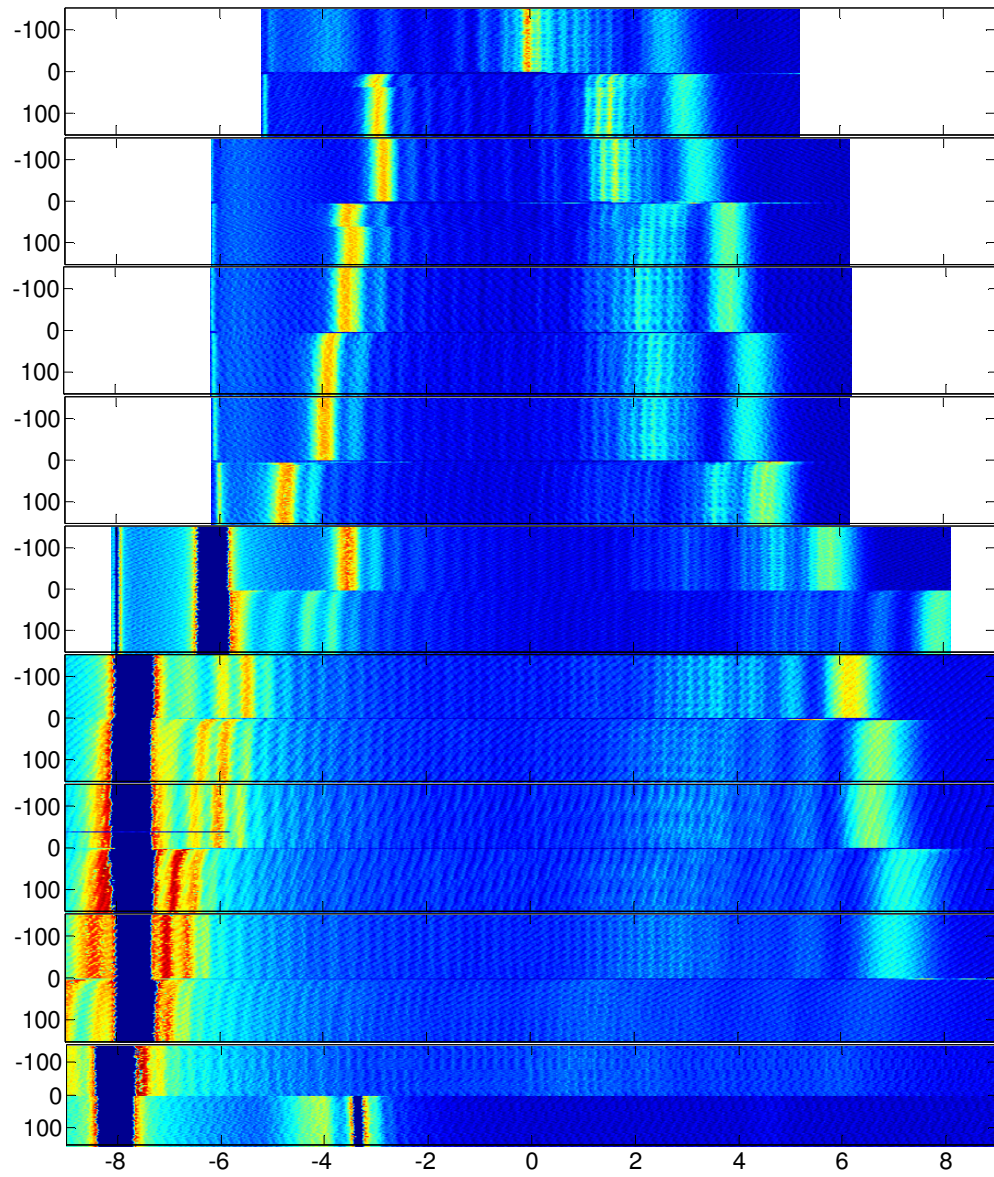


**Figure 3.48** Image of responses for strikes 14 through 22 (from top to bottom) for sample BY-4 showing secondary response at wavelengths several nanometers longer than the primary response. Each image shows 125ms before and 125ms after the initial FBG response during the strike event. The horizontal axes show wavelength shift (nm) from an initial reference point prior to damage..

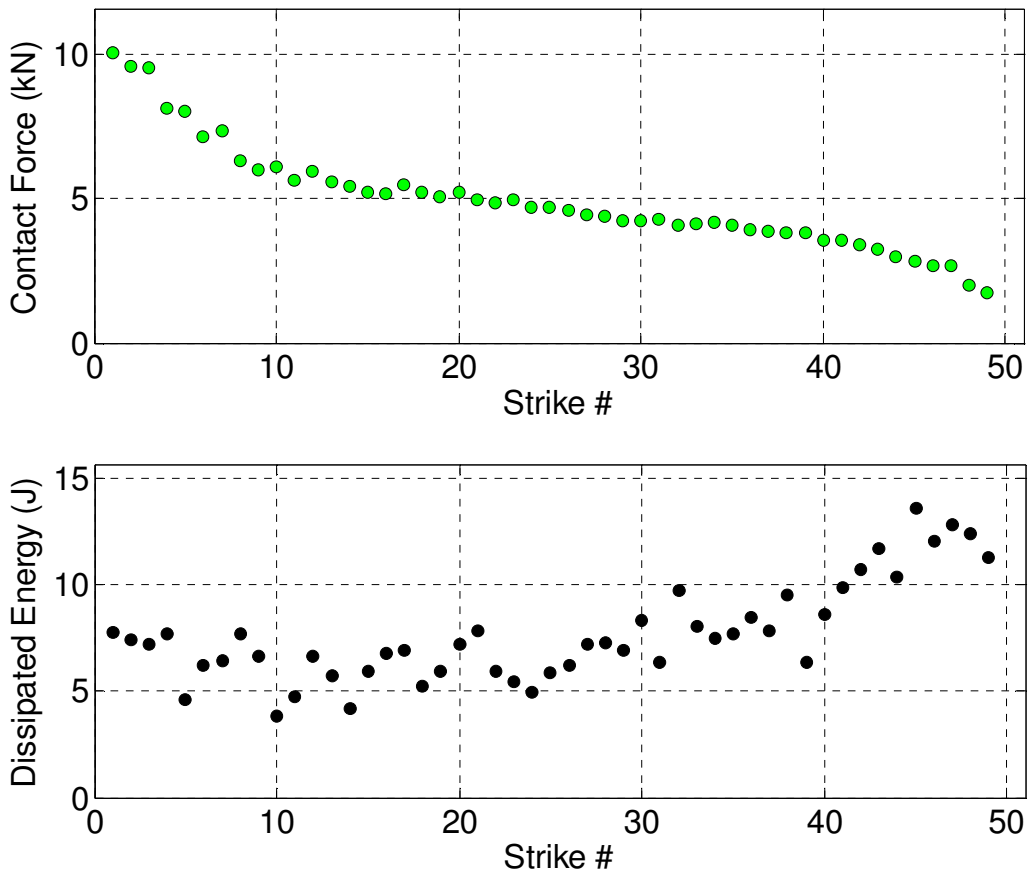


Figure 3.49 Contact force between impactor and the sample (top) and energy dissipated over the life of the sample (bottom) for BY-4.

## Chapter 4. Conclusions

This study showed the potential for damage monitoring in composite structures subject to low velocity impacts events by applying FBG interrogation techniques over a range of time scales. Single optical fiber sensors were embedded into carbon fiber/epoxy resin woven composites using a single-step cure process. These composite specimens were tested to failure using multiple low energy impacts, which were characterized by acceleration and position sensors integrated into the impactor head. The embedded FBG sensors were interrogated using three different interrogation techniques: low speed full spectrum via a tunable laser source, high speed peak wavelength detection via a commercial unit, and high speed full spectrum using instrumentation provided by Brigham Young University. By qualitatively examining the responses of these three techniques and comparing the FBG data with impact characterization data, a more complete picture of the composite damage progression can be created. Utilization of these techniques in combination with further improvements shows much potential for future SHM systems.

Conclusions to be drawn from analyzing the data using the three different FBG sensor interrogation techniques are the following:

- The changes in the residual strain state measured from the full spectral response of the FBG sensor correlated qualitatively to changes in the global maximum contact force and dissipated energy measures obtained from the same specimens.

- Measurement of the peak wavelength shift during the impact event could provide quantitative information on the initiation and progression of damage if higher data acquisition rates were achieved than presented in this work. The highly distorted spectra due to embedment and strain concentrations could still present a problem for some cases.
- Interrogation of the FBG sensor spectrum at acquisitions rates up to 926 Hz demonstrated that several spectral features previously observed in post-impact residual scans can also be seen to appear and disappear during the impact event including peak splitting and peak broadening.
- Interrogation of the FBG sensor spectrum at rates between 200 and 926 Hz also permitted the direct measurement of the transient response of the sensor during and immediately following the impact. This relaxation time increased throughout the lifetime of the composite due to a transfer of energy dissipation from fiber breakage and matrix cracking to the mechanisms of delamination and matrix deformations.
- Oscillations appearing in the FBG sensor spectra during the impact event during selected strikes indicated damage occurring in the form of rapid fiber breakage and matrix cracking.
- For selected specimens, resonant peaks appeared in the FBG sensor spectra that were several nanometers from the main resonance peaks, potentially due to super-structuring of the gratings through the woven architecture of the pre-preg material.

In order to utilize the interrogation techniques for real world SHM systems, a damage metric must be generated by apply quantitative analysis to the data gathered. Since the grating response incorporates distortion due to the fabrication and embedment processes, any method must be unaffected by the initial undamaged spectra. One method utilizes the undamaged grating response after embedment to form a baseline for correlation techniques. Subsequent spectra are compared with the original response and a correlation factor is generated for each point along the spectrum. This serves to filter the relatively noisy features of the embedded grating response. Future experimentation might identify a threshold correlation factor, below which failure of the composite is considered imminent.

## REFERENCES

- Capoluongo, P., Ambrossino, C., Campopiano, S., Cutolo, A., Giordano, M., Bovio, I., Lecce, L., Cusano, A.,** 2007, "Modal Analysis and Damage Detection by Fiber Bragg Grating Sensors," *Sensors and Actuators*, Vol. 133.
- Carmen, G. and Sendeckji, G.,** 1995, "Review of Mechanics of Embedded Optical Sensors," *Journal of Composites Technology and Research*, Vol. 17, No. 3.
- De Morais, W. A., Monteiro, S. N., d'Almeida, J. R. M.,** 2005, "Evaluation of Repeated Low Energy Impact Damage in Carbon-Epoxy Composite Materials," *Composite Structures*, Vol. 67.
- Erdogan, T.,** 1997, "Fiber Grating Spectra," *Journal of Lightwave Technology*, Vol. 15, No. 8.
- Garrett, R. C., Peters, K. J., Zikry, M. A.,** 2009, "In-situ Impact-induced Damage Assessment of Woven Composite Laminates Through a Fiber Bragg Grating Sensor Network," accepted by the *Journal of the Royal Aeronautical Society* June 2009.
- Huang, S., LeBlanc, M., Ohn, M. M., Measures, R. M.,** 1995, "Bragg Intragrating Structural Sensing," *Applied Optics*, Vol. 34, No.22.
- Kunzler, W., Newman, J., Wilding, D., Zhu, Z., Lowder, T., Selfridge, R., Schultz, S., Wirthlin, M.,** 2008, "Advanced FBG Sensing Through Rapid Spectral Interrogation," *Proceedings of SPIE*, Vol. 6933.
- Kunzler, W., Zhu, Z., Wirthlin, M., Selfridge, R., Schultz, S., Propst, A., Peters, K., Zikry, M.,** 2009, "High Repetition-rate Full-spectrum Interrogation of FBG Sensors for Dynamic Measurements in Composite Laminates," submitted to *Smart Materials and Structures*.
- Lloyd, P. A., Pressland, R., McFeat, J., Read, I., Foote, P., Dupuis, J. P., O'Brien, E., Reithler, L., Grondel, S., Delebarre, C., Levin, K., Boller, C., Biemans, C., Staszewski, W. J.,** 2004, "Structural Health Monitoring Evaluation Tests," in *Health Monitoring of Aerospace Structures: Smart Sensor Technologies and Signal Processing* by Staszewski, W. J., Boller, C., and Tomlinson, C. (ed), John Wiley & Sons, Hoboken, NJ.
- Lloyd, S. W., Newman, J., Parsons, E., Selfridge, R., Schultz, S.,** 2007, "A Fiber Sensor Integrated Monitor for Embedded Instrumentation Systems," *Review of Scientific Instruments*, Vol. 78.

- Measures, R. M.**, 2001, *Structural Health Monitoring with Fiber Optic Technology*, Academic Press, San Diego, CA.
- Othonos, A. and Kalli, K.**, 1999, *Fiber Bragg Gratings*, Archtech House, Norwood, MA.
- Pearson, J. D., Zikry, M. A., Prabhugoud, M., Peters, K.**, 2007, "Global-local Assessment of Low-velocity Impact Damage in Woven Composites," *Journal of Composite Materials*, Vol. 41.
- Takeda, N., Okabe, Y., Kuwahara, J., Kojima, S., Ogisu, T.**, 2005, "Development of Smart Composite Structures with Small-diameter Fiber Bragg Grating Sensors for Damage Detection: Quantitative Evaluation of Delamination Length in CFRP Laminates Using Lamb Wave Sensing," *Composites Science and Technology*, Vol. 65.
- Tsuda, H. and Lee, J.**, 2007, "Strain and Damage Monitoring of CFRP in Impact Loading Using Fiber Bragg Grating Sensor System," *Composites Science and Technology*, Vol. 67.
- Tsuda, H.**, 2006, "Ultrasound and Damage Detection in CFRP Using Fiber Bragg Grating Sensors," *Composites Science and Technology*, Vol. 66.
- Yashiro, S., Okabe, T., Takeda, N.**, 2007, "Damage Identification in a Holed CFRP Laminate Using a Chirped Fiber Bragg Grating Sensor," *Composites Science and Technology*, Vol. 67.
- Yigit, A. S. and Christoforou, A. P.**, 1994, "On the Impact of a Spherical Indenter and an Elastic-Plastic Transversely Isotropic Half-Space," *Composites Engineering*, Vol. 4.

## APPENDICES

## APPENDIX A – MATLAB Code for Reducing NCSU Drop Tower Position and Acceleration Sensor Impact Characterization Data

```

%%%%%%%%%%%%%%%%%%%%%%%%%%%%%%%%%%%%%%%%%%%%%%%%%%%%%%%%%%%%%%%%%%%%%%%%
%   Impact Characterization Data Reduction
%   Date:   24 June 2008
%   Author: Adam Propst
%   North Carolina State University
%%%%%%%%%%%%%%%%%%%%%%%%%%%%%%%%%%%%%%%%%%%%%%%%%%%%%%%%%%%%%%%%%%%%%%%%
close all; clear all; clc;

rootdir = ('C:\Users\Adam\Desktop\Research\Thesis Data\
           Data\2008-07-18_sample\Oscilloscope\');

name=dir(fullfile(rootdir, '*.csv'));

afilternum=5;           % Number of points to filter for acceleration data

for i=1:length(name)/2;
    strikes = length(name)/2;

    aname=name(i*2-1).name;           % Renames all accel data files
    accel{i}=dlmread(fullfile(rootdir,aname), ',', 'A24..B1024');
    pname=name(i*2).name;           % Renames all position data files
    pos{i}=dlmread(fullfile(rootdir,pname), ',', 'A24..B1024');

    % Filter acceleration data
    afilt{i}=filtfilt(ones(1,afilternum)/afilternum,1,accel{i});

    % Calculate initial velocity
    xin{i}=pos{i}(1:300,1);
    yin{i}=pos{i}(1:300,2)*0.228972;
    A{i}=[ones(length(xin{i}),1),xin{i}]\yin{i};
    vin(i)=A{i}(2,1);

    % Calculate exit velocity
    xout{i}=pos{i}(700:1000,1);
    yout{i}=pos{i}(700:1000,2)*0.228972;
    B{i}=[ones(length(xout{i}),1),xout{i}]\yout{i};
    vout(i)=B{i}(2,1);

    % Calculate change in kinetic energy and contact force
    KE(i)=0.5*5.5*(vin(i)^2-vout(i)^2);           % Dissipated energy
    CF(i)=5.5*100*9.81*max(afilt{i}(:,2));           % Max contact force
end;

```

## APPENDIX B – MATLAB Code for Reducing High Speed, Full Spectrum Data (BY-1)

```
% *****
% This program reduces the data collected for sample BY-1
% Date: 24 June 2008
% Author: Adam Propst
% North Carolina State University
% *****
close all; clear all; clc;

rootdir = 'C:\Users\Adam\Desktop\Research\Thesis Data\
          Data\2008-06-03_BYU_sample\BYU_data\
          raw_data\NCSU-BYU Data 03June2008\';

files = dir(rootdir);
numfiles = length(files);

for strike = 1:numfiles-3

    % Read in the raw data from a single strike file *****
    rawdata = csvread(fullfile(rootdir,getfield(files(strike+3), 'name')));

    % Filter data to reduce noise *****
    windowSize = 10; % set filtering window to 10 samples
    filtdata = filtfilt(ones(1,windowSize)/windowSize,1,rawdata);

    numpoints = 2500000;
    i = 1500000; % initialize index counter
    j = 1; % initialize sweep counter

    sweep = zeros(4000,100);

    % Loop to scan through all the frequency sweeps in the data file *****
    while (i < numpoints-10000)

        % Average several points *****
        locavg1 = filtdata(i+00);
        locavg2 = filtdata(i+02);
        locavg3 = filtdata(i+04);
        locavg4 = filtdata(i+06);
        locavg5 = filtdata(i+08);
        locavg = (locavg1+locavg2+locavg3+locavg4+locavg5)/5;

        if (locavg > 0.35) % locavg indicates reference FBG
            % Store data as a single frequency sweep with 4000 points
            for n = 1:4000
                sweep(n,j) = rawdata(i-500+n); % Store embedded FBG pts
            end
        end
    end
end
```

```

end

% Store trigger data as a single frequency sweep with 100 pts
for n = 1:100
    trigger(n,j) = filtdata(i+n); % Store ref FBG pts
end

    j = j+1; % increase sweep counter
    i = i+9000; % move index next to reference sensor
end

    i = i+1; % increase index counter
end

Raw_data = sweep';

save([rootdir, 'Reduced_data\', num2str(strike)], ...
    'rawdata', 'Raw_data', 'trigger', 'windowSize');

end

```

## APPENDIX C – MATLAB Code for Reducing High Speed, Full Spectrum Data (BY-2 – BY-4)

```
% *****
% This program reduces the data collected for samples BY2-BY4
% Date: 18 August 2008
% Author: Adam Propst
% North Carolina State University
% *****
clear all; close all; clc

rootdir = ('C:\Users\Adam\Desktop\Research\Thesis Data\Data\
          2008-08-07_BYU_sample\Sample1\BYU_data\');

folders = dir(rootdir);
numfolders = length(folders);

for strike = 5:(numfolders-4)

    files = dir([rootdir,getfield(folders(strike+4), 'name')]);
    numfiles = length(files);

    if (numfiles<3)
        continue
    end

    for data_set = 1:(numfiles-2)

        filename = fullfile(rootdir,getfield(folders(strike+4), 'name'), ...
                             getfield(files(data_set+2), 'name'));
        fid = fopen(filename);

        len=1501;
        Raw_data=[];
        Raw_time=[];
        Raw_start=[];
        Raw_len=[];
        for loop=1:10000
            loop;

            % read in characters until 'timestamp' *****
            if feof(fid)==1
                break
            end

            S='time';
            C = fread(fid,1, 'char');
            tmp0=char(C);
```

```

C = fread(fid,1,'char');
tmp0=[tmp0,char(C)];
lp=1;

while ~strncmp(tmp0,S,2)
    lp=lp+1;
    C = fread(fid,1,'char');
    tmp0=[tmp0(2),char(C)];
    %char(C)
end

%go to the end of the word
C = fread(fid,1,'char');
%char(C)
lp=1;
while char(C)~=':'
    lp=lp+1;
    C = fread(fid,1,'char');
    %char(C)
end

if feof(fid)==1
    break
end

%read in the timestamp
C = fread(fid,1,'char');

%char(C)
tmp1=[];
lp=1;
while char(C)~='s'
    lp=lp+1;
    C = fread(fid,1,'char');
    tmp1=[tmp1,char(C)];
end

if feof(fid)==1
    break
end

tim=str2num(tmp1(1:end-1));

% read in characters until 'waveform_start' *****
S='st';
C = fread(fid,1,'char');
tmp0=char(C);
C = fread(fid,1,'char');
tmp0=[tmp0,char(C)];
lp=1;
while ~strncmp(tmp0,S,2)

```

```

        lp=lp+1;
        C = fread(fid,1,'char');
        tmp0=[tmp0(2),char(C)];
        %char(C)
end

if feof(fid)==1
    break
end

%go to the end of the word
C1 = fread(fid,1,'char');
%char(C1)
lp=1;
while char(C1)~=':'
    lp=lp+1;
    C1 = fread(fid,1,'char');
    %char(C1)
end

if feof(fid)==1
    break
end

%read in the waveform_start
C1 = fread(fid,1,'char');
%char(C1)
tmp2=[];
lp=1;
while char(C1)~='w'
    lp=lp+1;
    C1 = fread(fid,1,'char');
    tmp2=[tmp2,char(C1)];
end

if feof(fid)==1
    break
end

start=str2num(tmp2(1:end-2));

% read in characters until 'waveform_length' *****
S='le';
C = fread(fid,1,'char');
tmp0=char(C);
C = fread(fid,1,'char');
tmp0=[tmp0,char(C)];
lp=1;
while ~strncmp(tmp0,S,2)
    lp=lp+1;
    C = fread(fid,1,'char');

```

```

        tmp0=[tmp0(2),char(C)];
        %char(C)
end

if feof(fid)==1
    break
end

%go to the end of the word
C1 = fread(fid,1,'char');
%char(C1)
lp=1;
while char(C1)~=':'
    lp=lp+1;
    C1 = fread(fid,1,'char');
    %char(C1)
end

if feof(fid)==1
    break
end

%read in the waveform_length
C1 = fread(fid,1,'char');
%char(C1)
tmp2=[];
lp=1;
while char(C1)~='p'
    lp=lp+1;
    C1 = fread(fid,1,'char');
    tmp2=[tmp2,char(C1)];
end

if feof(fid)==1
    break
end

len=str2num(tmp2(1:end-2));

% read in characters until 'waveform_intensity_data' *****
S='da';
C = fread(fid,1,'char');
tmp0=char(C);
C = fread(fid,1,'char');
tmp0=[tmp0,char(C)];
lp=1;
while ~strncmp(tmp0,S,2)
    lp=lp+1;
    C = fread(fid,1,'char');
    tmp0=[tmp0(2),char(C)];
    %char(C)

```

```

end

if feof(fid)==1
    break
end

%go to the end of the word
C2 = fread(fid,1,'char');
%char(C)
lp=1;
while char(C2)~=':'
    lp=lp+1;
    C2 = fread(fid,1,'char');
    %char(C2)
end

if feof(fid)==1
    break
end

%read to eliminate return
C2 = fread(fid,1,'char');
%char(C)

%read in binary data
Data = fread(fid,len,'uint16');

%check for partial scan
if (length(Data) < len)
    break %continue
end

if (feof(fid) == 1)
    break
end

ii=find(Data>1000);
Data(ii)=zeros(size(ii));
Raw_data(loop,:) = Data;
Raw_time(loop)=tim;
Raw_start(loop)=start;
end

fclose(fid)

voltage=Raw_start(1):Raw_start(1)+len-1;
b=1544.18+8e-3*11500;
lambda=-8e-3*voltage+b;

```

%%%

```
if (strike < 10)
  save([rootdir, 'Reduced_data\', '0', num2str(strike), '_', ...
        num2str(data_set)], 'Raw_data', 'Raw_time');
else
  save([rootdir, 'Reduced_data\', num2str(strike), '_', ...
        num2str(data_set)], 'Raw_data', 'Raw_time');
end
end
end
```

## APPENDIX D – MATLAB Code for Processing and Displaying High Speed, Full Spectrum Data

```

% *****
% This program processes data for sample BY-1 through BY-4
% Date: 26 August 2008
% Author: Adam Propst
% North Carolina State University
% *****
close all; clear all; clc;

% Create list of files to create images from and open file with locations
% of impact points in those files

rootdir = ('C:\Users\Adam\Desktop\Research\Thesis Data\Data\
          2008-06-03_BYU_sample\BYU_data\raw_data\
          NCSU-BYU Data 03June2008\Reduced_data\');

files = dir(rootdir);      % List of files in the root directory
numfiles = length(files); % Number of files in the root directory

uiopen;      % Open BY-#_impact_points.CSV file in main data folder
pause(10);   % Pause to allow user time to open impact_points.CSV file

% Main loop
for filenum = 1:numfiles-4
    load(fullfile(rootdir,getfield(files(filenum+2),'name')));

    scans = size(Raw_data,1);      % Num of freq sweeps in current file
    width = size(Raw_data,2);      % Num of data pts in each freq sweep

    %%%%%%%%%%%%%%%%%%%%%%%%%%%%%%%%%%%%%%%%%%%%%%%%%%%%%%%%%%%%%
    % Filter data to smooth out noise
    Filtered_data = zeros(scans,width);      % Allocate memory
    for i = 1:scans
        windowSize = 10;
        Filtered_data(i,:) = filtfilt(ones(1,windowSize)/windowSize,...
            1,Raw_data(i,:));
    end

    %%%%%%%%%%%%%%%%%%%%%%%%%%%%%%%%%%%%%%%%%%%%%%%%%%%%%%%%%%%%%
    % Pull subset from raw data
    X = 100;
    Y = 3000;
    data_window = zeros(X,Y);
    for i = 1:X
        for j = 1:Y

```

```

        data_window(i,j) = Filtered_data(i,j+data(filenum,4)-Y/2);
    end
end

%%%%%%%%%%%%%%%%%%%%%%%%%%%%%%%%%%%%%%%%%%%%%%%%%%%%%%%%%%%%%%%%%%%%%%%%
data_window(1,1) = 0.15;    % Set max intensity scaling
data_window(2,1) = -0.07;  % Set min intensity scaling

rate = 200/1000;           % Frequency scan rate (scans/ms)

figure('Position',[300 325 1000 800]);
set(figure(1),'Visible','off');
caxis([-0.07 0.15]);
pic = imagesc(data_window,'YData',[-(data(filenum,3))/rate...
    (100-data(filenum,3))/rate],'XData',[-data(filenum,4)/251...
    (Y-data(filenum,4))/251]); axis ij; hold on;

name = getfield(files(filenum+2),'name');

% Save image file
saveas(pic,[rootdir,'images\','BY-1_zoom_',name(1:2)],'jpg')
saveas(pic,[rootdir,'images\figures\','BY-1_zoom_',name(1:2)],'fig')

% Clear data sets
clear Raw_data;
clear Raw_time;
clear Filtered_data;
clear data_window;
close;
end

```